Convergent extension requires adhesion-dependent biomechanical integration of cell crawling and junction contraction

Shinuo Weng, Robert J. Huebner, and John B. Wallingford*

Department of Molecular Biosciences, University of Texas at Austin

*Correspondence to:

John Wallingford
Patterson Labs
2401 Speedway
Austin, Texas
78712
Wallingford@austin.utexas.edu
512-232-2784

Abstract:

Convergent extension is an evolutionarily conserved collective cell movement that elongates the body axis of all animals and is required for the morphogenesis of several organ systems. Decades of study have revealed two distinct mechanisms of cell movement during CE, one based on cell crawling and the other on junction contraction. How these two behaviors collaborate during CE is not understood. Here, using quantitative live cell imaging we show that these two modes act both independently and in concert during CE, but that cell movement is more effective when the two modes are integrated via mechano-reciprocity. Based on these findings, we developed a novel computational model that for the first time treats crawling and contraction independently. This model not only confirmed the biomechanical efficacy of integrating the two modes, but also revealed for the first time how the two modes -and their integration- are influenced by cell adhesion. Finally, we use these new insights to further understand the complex CE phenotype resulting from loss of the C-cadherin interacting catenin Arvcf. These data are significant for providing new biomechanical and cell biological insights into a fundamental morphogenetic process that is implicated in human neural tube defects and skeletal dysplasias.

Introduction:

Convergent extension (CE) is a fundamental collective cell movement in which a developing tissue converges along one axis, thereby extending in the orthogonal direction (**Fig. 1A**). CE plays a crucial role in embryogenesis by shaping the body axis during gastrulation and neurulation and by elongating tubular organs during organogenesis (Keller, 2002; Tada and Heisenberg, 2012). The cell movements of CE are evolutionarily conserved in animals ranging from nematodes and arthropods to vertebrates (Huebner and Wallingford, 2018). Moreover, failure of CE is associated with severe birth defects, including neural tube defects, heart defects, and skeletal dysplasias (Butler and Wallingford, 2017; Walck-Shannon and Hardin, 2014; Wallingford et al., 2013).

Two distinct cellular mechanisms for convergent extension have been described, and they were initially discovered in different cell types. The first was discovered by work on *Xenopus* body axis elongation during gastrulation (Keller and Hardin, 1987; Keller and Tibbetts, 1989; Shih and Keller, 1992). In this case, intercalation of mesenchymal cells is driven by polarized actin-based protrusions extending from the mediolateral (ML) vertices of cells (**Fig. 1B**) (Keller et al., 1992). These protrusions resemble a combination of the sheet-like lamellipodia and spike-like filopodia observed on the leading edge of cultured migrating cells (Devitt et al., 2021), pushing the boundary between cells (**Fig. 1B**). They also form adhesions with the substrate and with the neighboring cells, thus preventing protrusions from retracting and driving cell intercalation in a manner similar to cell migration (Keller and Sutherland, 2020; Pfister et al., 2016).

The second cellular mechanism was discovered in epithelial cells during *Drosophila* germband extension (Irvine and Wieschaus, 1994). In this case, cell intercalation is achieved via polarized junction remodeling, in which junctions joining anteroposterior (AP) neighbor cells shorten via actomyosin contraction (Bertet et al., 2004; Zallen and Wieschaus, 2004)(**Fig. 1C**). We will refer to these two distinct modes as the “crawling” and “contraction” modes, respectively (**Fig. 1B, C**).

The two modes were initially considered as distinct mechanisms that were implemented in either mesenchyme or epithelia (e.g. (Lienkamp et al., 2012; Nishimura et al., 2012)), cell types

that differ significantly in terms of cell-cell adhesion and cell polarity. However, recent evidence suggests that many cell types employ both modes during CE (Huebner and Wallingford, 2018; Shindo, 2018). For example, the two modes were found to work in conjunction in epithelial cells, first in the mouse neural plate, and later in the *Drosophila* germ band (Sun et al., 2017; Williams et al., 2014). In both cases, the crawling mode acts via basolaterally positioned protrusions, while contractions act apically at the epithelial junctions. Interestingly, we previously identified a role for the contraction mode in CE of mesenchymal cells of the *Xenopus* notochord (Shindo et al., 2019; Shindo and Wallingford, 2014), the very cells in which the crawling mode was first defined.

Together, these previous studies suggest that crawling and contraction modes may be integrated in some manner to confer a maximal biomechanical advantage. The nature of such integration is unknown. Here, we used quantitative live-cell microscopy and a novel computational model to demonstrate that cell crawling and junction contraction act both independently and collaboratively to drive CE in *Xenopus*. Furthermore, our modeling suggests that fine control of cell adhesion is essential for mechano-reciprocal integration of crawling and contraction, and experimental manipulation of the cadherin-interacting catenin Arvcf *in vivo* validated this prediction. These data provide new biomechanical and cell biological insights into a fundamental morphogenetic process implicated in human diseases and have broader impacts on studies of collective cell movement in various contexts.

Results & Discussion:

Direct quantification demonstrates that crawling and contraction modes of intercalation act both independently and in concert during vertebrate convergent extension

The mesenchymal cells of *Xenopus* gastrula mesoderm are a key paradigm for studies of the cell biology, molecular biology, and biomechanics of CE (Chu et al., 2020; Keller et al., 2003). Both crawling- and contraction-based cell intercalation mechanisms have been explored in this system, but how the two are coordinated remains unclear (Keller and Hardin, 1987; Keller and Tibbetts, 1989; Shih and Keller, 1992; Shindo et al., 2019; Shindo and Wallingford, 2014).

To directly assess the contributions of crawling and contraction, we imaged explants of the *Xenopus* dorsal marginal zone ("Keller" explants) that were uniformly labelled with the membrane marker memBFP, and mosaically labelled for different colors of an actin biosensor (Lifeact-RFP/Lifeact-GFP)(**Supp. Fig. 1**). This approach allowed us to use the uniform membrane-BFP to segment cells and to assess cell intercalation (**Fig. 1D**), while using Lifeact-GFP and -RFP to unambiguously quantify different populations of actin (**Fig. 1E, F**). Specifically, we analyzed three- and four-cell clusters in which actin in ML cells was labeled in one color and actin in AP cells in another color (**Fig. 1E, F**; **Supp. Fig. 1B**).

Actin dynamics are known to be pulsatile in both crawling and contraction modes (Kim and Davidson, 2011; Pfister et al., 2016; Shindo et al., 2019; Shindo and Wallingford, 2014). This property, as well as substantial heterogeneity, was apparent when we used kymographs to visualize actin dynamics at ML cell protrusions and AP cell interfaces (**Fig. 1G, H**; green and purple respectively). Kymographs also revealed that contraction pulses along an AP cell interface were largely restricted to the tricellular regions (tCR)(**Fig. 1H**) and were less pronounced in the middle portion of AP cell interface (**Fig. 1H**, Mid). We also observed that ML

actin dynamics of two cells separated by an AP junction were independent and unsynchronized (**Fig. 1G**).

To quantify crawling and contraction, we measured the changes in mean intensity of the distinct actin reporters labelling ML or AP cells (e.g. **Fig. 1E, F**; **Supp. Fig. 2A**). Details of our approach and justification for specific measurements made are described in the Methods section (and see **Supp. Fig. 3**). Briefly, we focused on ML and AP actin dynamics in tricellular regions (tCRs) and analyzed how they are related to cell intercalation as quantified by the displacement of tricellular vertices determined from the uniform memBFP signal (**Supp. Fig. 2B**).

We considered that crawling and contraction mechanisms could either “take turns” or work together, or both. To explore these possibilities, we took advantage of the pulsatile nature of both actin dynamics and cell movement during CE. We first used individual peaks in intercalation velocity curves over time to identify single intercalation “steps” (**Fig. 2A**, left). Then, for each step, we searched for cross-correlated peaks in ML and AP actin intensity within the 40-sec window preceding the velocity peak (**Fig. 2A**, right). This method allowed us to unambiguously associate each step of cell intercalation movement with crawling- and/or contraction-related actin dynamics.

In our data, we could clearly identify intercalation steps driven exclusively by cell crawling (i.e. correlated with a crawling peak in ML actin intensity) (**Fig. 2B**) as well as steps driven by contraction (i.e. correlated with a contraction peak in AP actin intensity)(**Fig. 2C**). In addition, we identified steps associated with paired peaks in both ML and AP actin intensity (**Fig. 2D, E**). These concurrent intercalation steps included cases in which a crawling peak precedes a contraction peak (**Fig. 2D**), and a similar number of cases in which a contraction peak precedes a crawling peak (**Fig. 2E**).

We were able to clearly assign a driving force to roughly 60 percent of all observed intercalation steps (**Fig. 2F**, left; **Supp. Fig. 4A**). Of these, we found that roughly one-third of all steps were associated purely with crawling, another third with contraction, and the final third with both (**Fig. 2F**, left). Intercalation steps are known to be highly heterogeneous, so it was notable that when we considered the step duration, rather than the number of steps, we again found an equal distribution of crawling, contraction, and concurrent steps (**Fig. 2F**, middle). By contrast, when we considered actual vertex displacement (i.e. the amount of cell intercalation), we found that concurrent steps accounted for far more than one-third of the distance moved by tricellular vertices (**Fig. 2F**, right). Together, these data affirm the complex relationship between crawling and contraction, and moreover, suggest that the two modes can be simultaneously integrated to produce more effective cell movement than can either mode acting alone.

Simultaneous integration of crawling and contraction improves the efficacy of cell intercalation

To further define crawling-only, contraction-only, and concurrent intercalation steps, we quantified several additional metrics. We found that the significantly higher displacement for concurrent steps (**Fig. 3A**) was related to an increased duration of the steps (**Fig. 3B**), and also to an increased velocity of vertex movement (**Fig. 3C**). Moreover, we noted that some steps involved multiple successively correlated crawling and contraction peaks (**Fig. 3D**; **Supp. Fig. 4A**, dagger), suggesting an iterative integration of crawling and contraction. We reasoned that if integration provided better efficacy, then iterative integration with multiple peaks should be more

productive. This was indeed the case, as intercalation accompanied by iterative integration exhibited significantly more displacement and a significantly longer duration than did those accompanied by only a single integration (**Fig. 3E, F**). Thus, concurrent crawling and contraction produces more effective movement by making each intercalation step both longer-lasting and faster than crawling-only or contraction-only steps.

Integration of concurrent crawling and contraction enhances actin assembly in both modes.

We next sought to understand how concurrent crawling and contraction produced more effective intercalation than does either mode alone. One possibility is biomechanical feedback of actomyosin networks. For example, previous studies in *Drosophila* suggest that tension generated by actomyosin contraction in one cell can stimulate actomyosin contraction in an adherent neighboring cell (e.g. (Fernandez-Gonzalez et al., 2009; Martin et al., 2010). To ask if a similar mechanism was at work here, we first compared contraction-related AP actin dynamics of contraction-only steps with that of AP actin during concurrent steps (**Fig. 4A**). Strikingly, both the peak intensity and the duration of AP actin pulses associated with concurrent steps were significantly higher than that in contraction-only steps (**Fig. 4B, C**).

We performed a complementary analysis of crawling-related ML actin dynamics (**Fig. 4D**), and we observed a similar trend; the peak intensity and duration of crawling protrusions were increased in concurrent events relative to crawling-only events (**Fig. 4E, F**). Thus, concurrent execution of crawling and contraction has a synergistic effect, enhancing actin assembly of both modes. This result suggest that the concurrent events are, in fact, integrated and moreover, suggest mechano-reciprocity that generates stronger forces during concurrent crawling and contraction (schematized in **Fig. 4G**).

A novel vertex model recapitulates integrated crawling- and contraction-based convergent extension

Theoretical modeling is a crucial tool in studies of morphogenesis, as it allows manipulation of attributes that may be difficult or impossible to manipulate experimentally, and several modeling studies have been used to explore the mechanics of convergent extension (e.g. (Alt et al., 2017; Fletcher et al., 2017; Merkel and Manning, 2017)). However, the vertex models commonly employed for such studies are limited, because *a)* they generally treat each cell-cell interface as a single homogeneous feature and *b)* they do not independently consider contributions from cell crawling and junction contraction (Belmonte et al., 2016; Brodland, 2006; Finegan et al., 2019; Shindo et al., 2019).

To overcome these limitations, we re-envisioned the vertex model of convergent extension. We represented each cell not as a six-vertex hexagon, but instead as a 90-vertex polygon, allowing us to model local events in discrete regions of individual cell-cell interfaces (**Fig. 5A**). Furthermore, cell-cell interfaces *in vivo* are formed of two apposed cell membranes, which are linked by cell-cell adhesion molecules but can behave independently. We therefore modeled junctions between two cells as two independent entities (**Fig. 5B**), while modeling cell adhesion to connect adjacent cells (**Fig. 5C**).

Details of the model are presented in the Methods, but briefly, we invoke three key forces: First, the pushing force for cell crawling was modeled as a defined force profile applied on tricellular

vertices (**Fig. 5D**, "F_{crawl}"). Second, the contractile force from actomyosin contraction pulses ("M_{pulse}") for junction contraction was modeled with Hill's muscle model (Mitrossilis et al., 2009a) (**Fig. 5E**, "$F_{contract}$"). Finally, we modeled the force transmitted between neighboring cells via force-dependent cell adhesion at cell interfaces using a catch-slip bond model (**Fig. 5C**, "$F_{adhesion}$", "$N_{adhesion}$"), which reflects the known role of Cadherin adhesion in convergent extension (Brieher and Gumbiner, 1994; Fagotto et al., 2013; Huebner et al., 2021a; Pfister et al., 2016). Without loss of generality, this model is dimensionless, but parameters for the key force components are estimated from experimental data, maintaining their relative values in a physiologically relevant range (Supp. Table.1).

Critically, our model successfully recapitulated many gross aspects of convergent extension. For example, we modelled cell intercalation using four-cell models (**Fig. 5F**). To reproduce actin dynamics observed *in vivo* (**Fig. 1G, H**), medially-directed crawling forces and contraction pulses were applied at random timepoints (**Supp. Fig. 5A, B**). This configuration consistently produced complete cell intercalation (i.e., "T1 transition"), including shortening of the AP cell interface and formation and elongation of a new AP directed cell-cell interface (**Fig. 5F**). Moreover, 27-cell clusters with both medially and laterally directed crawling forces applied to each cell at equal probability consistently recapitulated not just cell intercalation, but also tissue-wide convergent extension (**Fig. 5G**). Importantly, cells in the middle of the cluster, which were consistently restricted by their neighbors, were able to accomplish multiple rounds of cell intercalation (**Fig. 5G**). Thus, a combination of crawling and contraction in our novel model can recapitulate cell movements observed in vertebrate convergent extension *in vivo*.

Modeling recapitulates biomechanical synergy of crawling contraction integration

As a further test of our model's validity, we asked if it could also recapitulate finer-scale behaviors observed *in vivo*. To this end, we used four cell models to simulate shortening of AP interfaces, setting medially-directed crawling forces and AP actomyosin pulses in tCRs to defined time points so that we can distinguish crawling-only or contraction-only intercalation events from events with concurrent crawling and contraction (**Fig. 5H**). Importantly, we found that across a wide range of parameters for F_{crawl} and M_{pulse}, concurrent crawling and contraction in the model elicited greater vertex displacement and a higher mean vertex velocity (**Fig. 5I, J**; **Supp Fig. 6A, B)**, similar to the effects observed *in vivo* (**Fig. 3A, C**).

This finding prompted us to ask if our model also recapitulated the synergistic effect of crawling-contraction integration on actin assembly that we observed *in vivo* (**Fig. 4**). We defined effective protrusion intensity in our model as the integral of protrusion length over time and used it as a proxy for protrusion dynamics (**Supp. Fig. 5D**). We reasoned that this is a mechano-responsive measure for a given crawling force, reflecting the interaction between a protrusion and its adjacent cells by considering both protrusion extension and retraction (**Supp. Fig. 5D**). We found that when crawling and contraction occurred concurrently, the effective protrusion intensity was significantly higher than when a crawling force was applied alone (**Fig. 5K**). This effect held for a wide range of crawling forces and actomyosin pulses (**Supp. Fig. 6C, D**). Importantly, this mechano-reciprocity is similar to that observed *in vivo* (i.e. **Fig. 4D-F**), but was not explicitly designed in the model.

Similarly, our model imposed actomyosin pulses ("M_{pulse}") for contraction, and the corresponding contraction forces ("$F_{contract}$") can be estimated directly from the Hill's muscle model (see Method; example in **Supp. Fig. 5B, C**). Mechanical forces are known to promote

assembly of actomyosin structures, forming a feedforward loop in several contexts, including during CE (Fernandez-Gonzalez et al., 2009; Martin et al., 2010; Miao and Blankenship, 2020; Uyeda et al., 2011; Zaidel-Bar et al., 2015). We therefore used the calculated contraction force as a proxy for actin dynamics at the cell cortex. Over a wide range of crawling forces and actomyosin pulses, we observed increased contraction forces when crawling and contraction occurred concurrently (**Fig. 5L**, **Supp. Fig. 6E, F**), again suggesting a mechano-reciprocal integration of crawling and contraction similar to that observed *in vivo* (**Fig. 4A-C**).

Thus, our model recapitulated not only the tissue-scale and cell-scale convergent extension, but also the synergy of crawling/contraction integration for both cell intercalation and enhanced actin assembly. The synergistic effects observed both *in vivo* and *in silico* suggest a mechano-reciprocity between the two distinct populations of actomyosin that drive the crawling and contraction modes of CE.

Modeling predicts a pivotal role for regulated adhesion for integration of crawling and contraction

Our working models for crawling/contraction integration schematized in **Fig. 4G** suggested a strong dependency on cell adhesion for effective integration. Thus, we next examined the effect of cell adhesion by modulating the adhesion units available, $N_{adhesion}^{tot}$, while maintaining a constant, moderate crawling force, F_{crawl} and constant moderate actomyosin pulses, M_{pulse}. Interestingly, when we reduced adhesion by half, we still consistently observed complete, if slower, cell intercalation in 4-cell models (**Fig. 6A**). However, we also observed enlarged extracellular voids between cells, particularly in tricellular and quad-cellular regions, reflecting the effect of reduced cell adhesion (**Fig. 6A**, insets). More strikingly, when we simulated convergent extension in a 27-cell model with reduced adhesion, both cell intercalation and tissue-wide convergent extension were still observed but were substantially reduced (**Fig. 6B**). In particular, we noted that cells in the center of the clusters that were physically restricted by the neighboring cells were essentially immobile during the second half of the simulation (**Fig. 6B**, asterisks).

We then used the modeling approaches outlined above (i.e., **Fig. 5H**) to ask how modulation of adhesion impacts the integration of concurrent crawling and contraction. We found that effective protrusion intensity tended to increase as adhesion decreased (**Fig. 6C**), and more interestingly, that the synergistic effect of concurrent crawling-contraction steps on ML actin intensity was only observed when adhesion was in the medium-high regimes (**Fig. 6C**). In low-adhesion regimes, ML actin was actually diminished in concurrent steps as compared to crawling-only steps (**Fig. 6C**), suggesting a high dependence on adhesion for protrusions to form stable contact with the cortex of another cell. In contrast, there was a pronounced trend for the contraction force to decrease with adhesion but the synergistic effect on contraction force during concurrent steps was quite robust to changes in adhesion (**Fig. 6D**), suggesting a differential impact of adhesion and the transmitted force on contraction versus crawling.

The Arvcf catenin is essential for normal integration of crawling and contraction

Finally, we considered that this new quantitative understanding of the relationship between the crawling and contraction modes of CE might shed light on complex experimental loss-of-function phenotypes. For example, the Arvcf catenin is a C-cadherin/Cdh3-interacting protein that is required for *Xenopus* CE (Fang et al., 2004a), but its mechanism of action is poorly

defined. In a companion paper, we show that while loss of Arvcf disrupts axis elongation in embryos, it does not eliminate cell intercalation *per se* (Huebner et al., 2021b). Rather, this phenotype reflects a role for Arvcf in the generation of adequate tissue-scale pushing forces during CE (Huebner et al., 2021b). The cell biological basis for this phenotype is not well defined, so we used insights from our mosaic labelling and modeling data to better understand the function of Arvcf.

In live imaging experiments, Arvcf deficient cells (see methods) displayed the normal aligned and elongated morphology of control cells (**Fig. 7A**), though their average intercalation velocity was significantly reduced (**Fig. 7B**). Strikingly, mosaic labeling of actin to quantify crawling, contraction, and concurrent intercalation steps revealed that crawling-only and contraction-only steps were unchanged after Arvcf knockdown (**Fig. 7C**). In striking contrast, intercalation during concurrent steps was significantly reduced in the absence of Arvcf (**Fig. 7C, right**), suggesting a specific role for this catenin in the normal synergistic integration of crawling and contraction during concurrent steps.

Consistent with its role as a Cdh3-interacting protein, our companion paper found that loss of Arvcf elicits a small but significant reduction in cadherin levels at cell-cell interfaces and extracellular gaps were observed between cells (Huebner et al., 2021b), a phenotype that we predicted here in our *in silico* model with low adhesion (**Fig. 6A**).

Moreover, our model also suggests that reduced adhesion should specifically disrupt the synergy of integration on crawling-related actin assembly (i.e. ML protrusions (**Fig. 6C**), and we found the same effect after Arvcf knockdown. Specifically, Arvcf knockdown significantly reduced the synergistic increase in the duration and intensity of ML protrusions normally observed in concurrent intercalation steps (**Fig. 7D, E**). Loss of Arvcf did not have a similar effect on contraction-related actin (**Supp. Fig. 7**), as we observed *in silico* (**Fig. 6D**). Thus, *in silico* and *in vivo* observations, as well as experimental manipulation of cadherin adhesion, together suggest the precise control of cell adhesion plays a pivotal role in integrating cell crawling and junction contraction, which in turn is essential for effective convergent extension.

Conclusions

Here, we have combined live imaging and a new approach to modeling to explore the mechanisms by which two modes of cell motility collaborate to drive a crucial morphogenetic process in early vertebrate embryos.

Our live imaging approach allowed us to independently identify and quantify the actin assembly associated with crawling or contraction (**Fig. 1-3)**. By doing so, we show that when crawling and contraction occur concurrently during mesenchymal CE in *Xenopus*, actin assembly associated with both processes is enhanced (**Fig. 4**). This result is consistent with the mechanosensitive responses of actomyosin observed in *Drosophila* epithelial cells (e.g. (Fernandez-Gonzalez et al., 2009; Martin et al., 2010). Moreover, this enhanced actin assembly in turn is associated with significantly improved efficacy of cell intercalation. Our work in mesenchymal cells in *Xenopus* suggests that the crawling- and contraction-based intercalation mechanisms in epithelial cells (e.g. (Sun et al., 2017; Williams et al., 2014) may be similarly coupled.

In addition, our new approach to modeling of CE provides a substantial advance over previous models. It independently captures junction contraction, cell crawling, cell-cell adhesion, and also treats individual cell cortices independently from one another, allowing detailed description of subcellular behaviors. This is crucial as individual cell-cell junctions during CE display very local heterogeneities in their mechanical properties (Huebner et al., 2021a). Despite the substantial increase in the complexity of our model, it nonetheless recapitulates both gross and fine characteristics of vertebrate CE as observed *in vivo*. Given the model's ability to accurately predict the effect of modulating cell adhesion on fine-scale cell behaviors that can be validated *in vivo*, we feel this model will provide a very useful resource for the community.

Finally, the work provides important new insights into the role of cell adhesion in vertebrate CE. Though studied extensively in epithelial cells during *Drosophila* CE (e.g. (Levayer and Lecuit, 2013; Truong Quang et al., 2013), the role of cadherin adhesion in vertebrate gastrulation is still poorly understood. Recent work suggests a key role for cadherins in both crawling- and contraction-based intercalation (Huebner et al., 2021a; Pfister et al., 2016), but our work here further demonstrates that fine-tuning of adhesion is crucial for the integration of the two, which is itself essential for normal morphogenesis. Further exploration of cadherin adhesion and its role in integrating biomechanical forces that drive CE will be important.

Acknowledgements:

This work was supported by grants from the NICHD (R01HD099191;1R21HD103882). We would also acknowledge Dr. Daniel J Dickinson and Dr. Abdul Naseer Malmi-Kakkada for critical reading.

Figure legend

Figure 1. Mosaic labeling showing dynamics of distinct actin populations for crawling and contraction during convergent extension. (A) Model of convergent extension showing cells interdigitate in the ML direction to elongate the tissue in the AP direction. (A, anterior; P, posterior, ML, mediolateral). (B) Sketch showing crawling mode in a 4-cell model, with actin in ML protrusions in green. (C) Sketch showing contraction mode in a 4-cell model with actin at AP interfaces in purple. (D-F) Still images from a representative time-lapse movie showing in (D) membrane (blue), in (E) actin in the ML protrusions for crawling (green, arrowheads) and in (F) actin at AP interfaces for contraction (purple). Dashed lines mark cell-celli interfaces. Boxes indicate tricellular regions ("tCR") and the middle region ("Mid"), see text for details. (G, H) Kymograph along the interface between AP cells shows spatiotemporal dynamics of actin from the ML protrusions representing the "crawling" signal (G) and actin from the AP cells representing the "contraction" signal (H).

Figure 2. Direct quantification of crawling- and contraction-based cell intercalation during convergent extension. (A) Schematic showing the method for intercalation step analysis. Left, individual peaks on the trace of intercalation velocity are identified as intercalation steps. Right, each step is categorized based on its correlation with peaks in the crawling and/or contraction signals (green and purple, respectively). If an intercalation step is correlated with a peak in the crawling or contraction signal, it is categorized as a crawling only or contraction only intercalation step. If a step is correlated with a pair of crawling and contraction peaks, it is categorized as an "concurrent" step. (B-E) Examples of (B) crawling only, (C) contraction only, and (D, E) concurrent intercalation steps. Each shows traces, a schematic, and still frames from time-lapse data. Asterisks mark the correlated peaks of velocity, crawling, and/or contraction. (F) Quantification of the number, duration, and cell vertex displacement by crawling-only, contraction-only, and concurrent steps.

Figure 3. Simultaneous integration of crawling and contraction improves the efficacy of cell intercalation. (A) Violin plot demonstrating that concurrent steps produce greater intercalation than do crawling or contraction steps. (B, C) Violin plots demonstrating that concurrent steps increase both the step duration and step velocity. (D) Sketch showing continuous integration ("2+ Integ.") when multiple sequentially correlated peaks in crawling and contraction signals are involved. (E, F) Violin plots demonstrating that continuous integration further improves the intercalation displacement and velocity.

Figure 4. Integration of crawling and contraction enhances actin assembly. (A) Schematic showing contraction pulses in contraction-only and concurrent conditions. (B, C) Violin plots showing increased peak actin intensity (B) and pulse duration (C) of contraction pulses when they occurred concurrently with crawling pulses compared with contraction pulses occurred alone. (D) Schematic showing crawling protrusions in crawling-only and concurrent conditions. (E, F) Violin plots showing increased peak actin intensity (E) and pulse duration (F) of crawling protrusions when they occurred concurrently with contraction pulses compared with crawling protrusion occurred alone. (G) Schematic showing enhanced actin assembly in crawling protrusions and contraction cortex when they are integrated.

Figure 5. A novel vertex model provides insights into the biomechanics of crawling-contraction integration. (A) Each individual cell was modelled as a 90-vertex polygon. (B) Explained in a 4-cell model, cell-cell interface was modeled as two independent entities. (C-E) Schematic focused on the boxed region in (B), showing the design modeling subcellular behaviors. (C) Cell-cell interfaces were connected via cell adhesion clusters of $N_{adhesion}$, holding

adhesive forces of $F_{adhesion}$. (D) Crawling forces F_{crawl} were applied to ML vertices around tricellular regions. (E) Contraction forces $F_{contraction}$ were added to cell cortex, which is a function of the amount of actomyosin density including actomyosin pules M_{pulse}. (F) Representative simulation result of a 4-cell model, showing not only the AP interface shortening, but also a new ML interface growing. (G) Representative simulation result of a 27-cell model, showing not only cell intercalation but also tissue-wide convergent extension. Highlighted cells in the middle of the cluster underwent multiple rounds of cell intercalation throughout the whole simulation. (H) Schematic showing timepoints for crawling forces and contraction pulses so that crawling-only or contraction-only intercalations steps can be distinguished from concurrent ones. (I, J) Violin plots showing the model recapitulates enhanced intercalation displacement and higher velocity for concurrent steps as compared to crawling or contraction alone. (K, L) Violin plots showing synergistic effect of integration on protrusion assembly (K) and AP contraction (L), recapitulating experimental observations (see Fig. 4).

Figure 6. Cell adhesion is critical to integrating crawling and contraction. (A) Representative simulation result of a 4-cell model with low adhesion. Slower AP interface shortening and ML junction growing were often observed. Inserts showing enlarged voids in tri-cellular and quad-cellular regions. (B) Representative simulation result of a 27-cell model with low adhesion. Asterisks make cells in the middle of the cluster that were stuck in the second half of the simulation. (C) Changes of effective protrusion intensity with adhesion. With each adhesion value, protrusions in crawling-only steps and concurrent steps are compared. “(WT)” marks the parameter used for simulating the wildtype condition in Fig. 5. (D) Changes of contraction force with adhesion. With each adhesion value, contraction force in contraction-only steps and concurrent steps are compared.

Figure 7. The Arvcf catenin is specifically required for integration of crawling and contraction. (A) Still images of membrane-GFP labelled cells in Keller explants, both wildtype control and Arvcf morphants display normal mediolateral polarization. (B) Bar plot showing the average intercalation velocity in wildtype and Arvcf knockdown cells. (C) Violin plots showing the vertex displacement in different types of intercalation steps, comparing wildtype and Arvcf knockdown cells. (D) Synergistic effect of integration on protrusion duration is eliminated by Arvcf knockdown. (G) Synergistic effect of integration on the intensity of ML actin assembly is reduced by Arvcf knockdown.

Supplementary figure legend

Supp. Figure 1. Mosaic labeling of actin to distinguish crawling and contraction signals at cell interfaces. (A) Schematic illustrating mosaic labelling. LifeAct-RFP and membrane-BFP mRNAs are injected into the left dorsal blastomere of 4-cell stage embryos, and LifeAct-GFP and membrane-BFP mRNAs into the right dorsal blastomere. (B) Representative images showing mosaic labeling of neighboring cells. Asterisks mark the tCRs where actin in the AP cells and actin in the M/L cell are labeled with different biosensors. Scalebar, 10 μm.

Supp. Figure 2. Quantification method for actin dynamics and cell intercalation. (A) Representative data illustrating quantification of actin dynamics. (a1) Membrane labeling was used for segmentation (blue) and cytosolic masks were generated for the quantification of cytosolic fluorescence background (gray). (a2, a3) Actin in the ML cells (a2) and in the AP cells (a3). Cell-cell interfaces were automatically detected using the membrane labeling (white dashed lines). tCRs where protrusions from the left (L) or right (R) cell colocalized with the AP interface were marked with white boxes. The middle region of the AP interface was also boxed for the quantification of contraction signal from the middle of the junction. (a4) Background cytosolic intensity of actin was defined as the mean actin intensity in a2 & a3 inside the regions marked with the cytosolic masks in a1 (solid lines). Their moving average over 6 min was taken and used for normalization (black dashed lines). (a5) The mean fluorescence intensity of actin in the boxed regions in (a2, a3). (a6) Fluorescence intensity normalized by the moving average of background intensity. (B) Schematic illustrating the quantification of cell intercalation. Dashed blue lines and solid blue lines are the cell-cell interfaces at two adjacent time points t_{i-1} and t_i. Black arrow shows the displacement vector of the tricellular vertex. Red arrow is the displacement along the AP interface at t_i (in-plane displacement), which contributes to cell intercalation. Gray arrow is the transverse displacement that does not contribute to cell intercalation.

Supp. Figure 3. Cross-correlation between cell intercalation velocity, crawling signal, and contraction signal. (A) Cross correlation between cell intercalation velocity for paired tricellular vertices (left) and the distribution of the maximum cross correlation coefficient. n = 8. (B) Cross correlation between the contraction signal from the tCR and that from the Mid region of the junction (left) and the distribution of the maximum cross correlation coefficient (right). n = 50. (C, D) Cell intercalation velocity of the left and right tricellular vertices in **Fig.1D-H** and the normalized crawling and contraction signals from the same sample. (E-G) Cross-correlation between cell intercalation velocity, crawling signal, and contraction signal. Each line represents cell intercalation at one tCR. Solid lines, the left tCR in Fig.1D-H; dashed lines, the right tCR in **Fig.1D-H**; gray lines, all other tCRs in the data set. n = 57.

Supp. Figure 4. Classification of intercalation steps. (A) Intercalation step analysis for the tCRs in **Fig. 1D-H**. For each tCR, the intercalation velocity, crawling signal, and contraction signal in the tCR were plotted verses time. Peaks and valleys were detected using customized scripts and individual peaks were separated with dashed lines at the adjacent valleys. An intercalation step was defined as an individual peak on the velocity trace and was classified based on its cross-correlation with pulses on the crawling and/or contraction signals. The correlated peaks were color-coded according to the figure legend. Intercalation steps that had no cross-correlation with crawling nor contraction pulses were filled with diagonal strips, while contraction and crawling pulses that had no cross-correlation with any intercalation step were filled with dots. Red arrows labelled correlated contraction and crawling pulses. Red double-line arrows marked correlated crawling and contraction pulses that are associated with different velocity peaks. Daggers marked crawling and contraction pulses that were correlated

successively. Lag-time window for all cross-correlation analysis was 40 sec, and the threshold for cross-correlation coefficient was 0.5. (B) Examples showing cell intercalation driven by contraction from the middle of the AP interface. (C) **Fig. 2F** replotted when contraction from the middle of the AP interface were also considered.

Supp. Figure 5. Design of crawling and contraction in a four-cell model. (A) Schematic showing the application of crawling force F_{crawl} and actomyosin pulses M_{pulse}. Crawling forces on the left and right cells were applied on the tricellular vertices at random timepoints and toward each other exclusively. Actomyosin pulses were applied at both tricellular regions and the middle of the AP interface. (B) Representative simulation input of crawling force and actomyosin pulses. Green traces show the profile of crawling forces on the left and right tricellular vertices. Magenta kymograph shows the spatiotemporal dynamics of the applied actomyosin pulses along the shortening AP interface. (C) Simulation output from the input in (B). Magenta kymograph shows the calculated contraction forces along the AP interface. Green traces mark the tip of the protrusions from the left and right cells. (D) Schematic showing the definition of the proxy for protrusion actin assembly. Depending on the cell-cell interaction, protrusion profile varies with the same applied crawling force. The integral of protrusion length over time, defined as the effective protrusion intensity, was used as a proxy for the protrusion actin assembly dynamics.

Supp. Figure 6. Biomechanical synergy of crawling contraction integration over a wide range of crawling forces and contraction pulses. (A) Effect of increasing crawling force on intercalation (vertex displacement) during crawling only, contraction only, and concurrent steps in the model. (B) Effect of increasing contraction on intercalation (vertex displacement) during crawling only, contraction only, and concurrent steps in the model. (C, D) Synergistic effect of crawling and contraction integration on the protrusion dynamics over a wide range of crawling forces and contraction pulses. (E, F) Synergistic effect of crawling-contraction integration on the contraction force over a wide range of crawling forces and contraction pulses. (WT) marks the parameters used for simulating the wildtype condition.

Supp. Figure 7. Contraction actin dynamics on cells lack of Arvcf. (A, B) Synergistic effects of integration on contraction duration (A) and intensity (B) were unaffected by Arvcf knockdown.

Supplementary table legend

Supp. Table 1. Parameters for the CE vertex model. Asterisks mark values used to simulate the wildtype condition, and dagger mark the value used to simulate the low adhesion condition.

Methods:

***Xenopus* embryo manipulations:** Ovulation was induced by injecting adult female Xenopus laevis with 600 units of human chorionic gonadotropin (HCG, MERCK Animal Health) and animals were kept at 16 dc overnight. Eggs were acquired the following day by squeezing the ovulating females and eggs were fertilized *in vitro*. Eggs were dejellied in 2.5% cysteine (pH 7.9) 1.5 hours after fertilization and reared in 1/3x Marc's modified Ringer's (MMR) solution. For micro-injection, embryos were placed in 2% ficoll in 1/3x MMR during injection and washed in 1/3x MMR 30 min after injection. Embryos were injected in the dorsal blastomeres at the 4-cell stage targeting the C1 cell at 32-cell stage and presumptive notochord. Keller explants were dissected at stage 10.25 in Steinberg's solution using hair tools.

Plasmids and Morpholinos: The Arvcf morpholino has been previously described (5'-ACACTGGCAGACCTGAGCCTATGGC-3' (Fang et al., 2004)) and was ordered from Gene Tools, LLC. Lifeact-GFP and Lifeact-RFP were made in pCS and membrane-BFP in pCS2.

mRNA and morpholino microinjections: Capped mRNA was generated using the ThermoFisher SP6 mMessage mMachine kit (Catalog number: AM1340). mRNAs were injected at the following concentrations per blastomere: Mem-BFP (75 pg), Lifeact-RFP (75 pg), and Lifeact-GFP (75 pg). Arvcf morpholino was injected at a concentration of 30ng per blastomere.

Imaging *Xenopus* explants: Explants were submerged in Steinberg's solutions and cultured on glass coverslips coated with Fibronectin (Sigma-Aldrich, F1141) at 5 μg/cm^2. After 5-hour incubation at room temperature, we started standard confocal time-lapse imaging using a Nikon A1R. Images of membrane-BFP, Lifeact-GFP, and Lifeact-RFP were taken at a focal plane 5 μm deep into the explant and at an interval of 10 sec.

Cell segmentation: All image process and analysis were performed using customized MATLAB scripts if not mentioned otherwise. We first performed cell segmentation and junction detection on images of Mem-BFP. Briefly, we used pixel classification in ilastik (Berg et al., 2019), a machine-learning based open-resource image analysis tool, to classify pixels at cell-cell interface and pixels in cytoplasm. This process converted a time-lapse movie of fluorescence intensity images to a time-lapse movie of probability images for cell-cell interface. We then extracted skeletons where the probability peaks, at each timepoint for a robust detection of cell-cell interfaces and cell segmentation.

Kymograph preparation: We customized the preparation of kymograph so that it not only displays actin fluorescence intensity values from crawling (ML cells) or contraction (AP cells) signals but also displays the movement of tricellular vertices explicitly. Briefly, we extracted 2 μm thick bands along the AP cell interface from images of actin labeling, linearized the bands, calculated the normalized mean fluorescence intensity across the thickness, then stacked data from each timepoint along the time axis. For a direct display of tricellular vertex movement, we used in-plane displacement at each time point, defined in **Supp. Fig. 2B**, as a reference to align the kymograph.

Measurement of cell intercalation: We defined cell intercalation as the displacement of a tricellular vertex along the direction to shorten the AP interface (**Supp. Fig. 2B**). Each tricellular vertex was tracked over time on the segmented images and its displacement in the tangential direction of the AP interface ("in-plane") between adjacent timepoints was quantified. (**Supp. Fig.2B**). The in-plane displacement is the only component that contributes to cell intercalation and junction shortening. The transverse movement of a tricellular vertex causes junction rotation

and was neglected here. The use of vertex displacement rather than the length of the AP cell interface for the quantification of cell intercalation was justified in **Supp. Fig. 3A**. The movement of vertices associated with the same AP cell interface was poorly correlated (**Supp. Fig. 3A)**, suggesting that their movement are independent with independent driving forces.

Measurement of crawling and contraction signals: For the quantification of actin intensity associated with crawling or contraction, a 2 μm thick band along the AP cell interface was extracted from the fluorescent image of actin for ML cells or AP cells respectively (**Supp. Fig. 2A.a2&3**). For each time point, we divided such bands into tricellular regions (tCRs) and the middle region (Mid) for the analysis of regional actin dynamics. The tCRs have a minimum length of 4 μm at any time point and covered the entire protrusions from the mediolateral cells if there were any. The middle regions were complementary to the tCRs and had a minimum length of 2 μm (**Supp. Fig. 2A.a2&3**). The raw crawling and contraction signals for cell intercalation were the average actin fluorescence intensity in the correspondence tCRs or the middle region when specified (**Supp. Fig. 2A.a5**). The necessity for such a regional analysis is apparent, since actin dynamics are highly heterogeneous long the AP interface (**Fig. 1G, H**). The low correlation between the contraction signal in a tCR and that in the adjacent middle region also supports this reginal analysis (**Supp. Fig. 3B**). Since contraction from the middle region of a junction has minor contribution to cell intercalation (**Supp. Fig. 4C**), this manuscript focuses on actin dynamics in tCRs and contraction signals refer to contraction in tCRs if not otherwise specified.

Normalization of fluorescence intensity signals: To allow for comparison of fluorescence intensity from different cells and from different actin biosensors, we normalized the fluorescence intensity of each cell with its mean cytosolic background intensity. Briefly, we used cell segmentation mentioned earlier to generate a cytosolic mask for each cell which excluded cell-cell interface and cell cortex with a 3 μm margin (**Supp. Fig. 2A.a1**). The mean fluorescence intensity within each cytosolic mask was quantified and its moving average over 6 min was calculated and used for normalization (**Supp. Fig. 2A.a4-a6**).

Intercalation step analysis by correlating actin dynamics and cell movement: To understand the underlying mechanisms for cell intercalation, we first performed cross-correlational analysis between the vertex velocity traces and the associated actin dynamics from the crawling or contraction signals in tCRs (**Supp. Fig. 3C-D**). The low cross correlation between the cell movement and actin dynamics (**Supp. Fig. 3E, F**) suggested a more complex mode of cell intercalation than crawling or contraction alone. Meanwhile, the contraction signals and crawling signals in tCRs were better correlated in over half of the cases (**Supp. Fig. 3G**), suggesting an active integration between them.

To infer the driving force for cell intercalation at a finer temporal resolution, we took the advantage of the pulsatile nature of both actin dynamics and cell movement during CE. We first identified peaks in the intercalation velocity curves as single intercalation “steps”, then searched for cross-correlated peaks in the crawling and contraction signals from tCRs within a 40-sec window preceding the velocity peak (**Fig. 2A, Supp. Fig. 4A**; threshold for cross-correlation: 0.5). If an intercalation step is correlated with a peak in the crawling or contraction signal, it is categorized as a crawling or contraction intercalation step (**Fig. 2B, C**). If an intercalation step is correlated with a pair of contraction and crawling peaks, it is categorized as a concurrent intercalation step (**Fig. 2D, E**). Within the 40-sec window, we observed comparable number of cases when a crawling peak precedes a contraction peak (**Fig. 2D**) and cases when a contraction peak precedes a crawling peak (**Fig. 2E**). Besides the crawling, contraction, and concurrent intercalation steps, which are the major players, we also observed intercalation steps

that are correlated with contraction peaks from the middle region of an AP interface (**Supp. Fig. 4B**). Compare with actin dynamics in tCRs, contraction in the middle region has much less contribution to cell intercalation (**Supp. Fig. 4C**).

Statistical analysis: For intercalation analysis, 57 vertices from wildtype cells from at least 10 independent experiments and 27 vertices from Arvcf KD cells from at least 3 independent experiment are pooled. For box plots, each dot represents a datapoint from a vertex. The central line is the median, the box extends vertically between the 25th and 75the percentiles, and the whiskers extend to the lower and upper limits that do not include the outliers. P values are calculated using two-sample t-test (MATLAB statistics toolbox). For violin plots, each dot represents an individual intercalation step/event (as in **Fig. 3**, **Fig. 5I, J**, and **Fig. 7C**), or an individual crawling or contraction pulse (as in **Fig. 4**, **Fig. 5K, L**, **Fig. 6C, D**, and **Fig. 7D, E**) identified from the data pool. Besides the included boxes, the violin plots also show the probability density extending from the lower limits to the upper limits that do not include the outliers. P values for violin plots are calculated using the two sample Kolmogorov-Smirnov test (MATLAB statistics toolbox). *p<0.05; **p<0.005; ***p<0.0005; N.S., not significant.

Vertex model to simulate convergent extension: To study how crawling and contraction act in concert to drive convergent extension, we designed a novel cell-based CE model that offers a detailed description of subcellular behaviors and allows for cells taking an arbitrary shape under subcellular forces. The design of the model is inspired by a cell-based model for the gastrulation of Nematostella vectensis (Tamulonis et al., 2011). Each cell is initially a hexagon and is represented by a 90-vertex polygon (**Fig. 5A**). Interfaces between any neighboring cells are allowed to connect via cell-cell adhesion (**Fig. 5B, C**).

The dynamics of the model is driven by simple Newtonian mechanics with the basic assumptions: (1) vertices are embedded in viscous medium that applies a viscous dragging force with the damping parameter η and (2) inertia vanishes. This leads to the governing equation for the evolution of the position $\boldsymbol{x_i}$ of vertex i determined by

$$\eta \frac{d\boldsymbol{x}i}{dt} = \boldsymbol{F_i}$$

, where $\boldsymbol{F_i}$ is the total force acting on the vertex *i*. Each simulation step is run by determining the forces acting on each vertex and solving the system of first-order differential equations using two-step Adam-Bashforth method with timestep $\Delta t = 0.05$. For each cell, vertices are reset every unit time so that each segment has relatively the same length and regions with high contraction do not have vertices over-crowded.

Inspired by the experimental observations, we considered three key force components in our model: (i) pushing force on the "leading" edge simulating lamellipodia and filopodia-like protrusions ("F_{crawl}", **Fig. 5D**), (ii) contractile force on cell edges simulating contraction at cell cortex ("$F_{contract}$", **Fig. 5E**), and (iii) adhesive force between cells simulating cadherin dependent cell adhesion ("$F_{adhesion}$", **Fig. 5C**). Secondary force components incorporated into our model include (iv) elastic cytosolic pressure maintaining the area of a cell and (v) repulsive force between cells to avoid cell collision. Without loss of generosity, this model is a dimensionless, but parameters for the key force components are estimated from experimental data, maintaining their relative values in a physiological relevant range (Supp. Table.1).

(i) Pushing force for cell crawling and protrusion extension.

We considered two force components associated with the crawling force, F_{crawl}, one for lamellipodia-like pushing on the "leading" edge and one for filopodia-like pushing at a more focused region. The "leading" edge forms stochastically and polarity-dependently (i.e., randomly toward median or lateral for convergent extension). Small pushing forces with a cosinusoidal profile and the maximum magnitude of F_l are applied on vertices along the leading edge for a period of T_l. The cosinusoidal force profile is initially centered around the anteroposterior center of the cell and could be shifted toward a protrusion when one forms as described below. Filopodia-like protrusions form stochastically on vertices in the tricellular regions on the "leading" edges. When a protrusion site is identified, a quartile-sine force pulse with the magnitude of F_p and the duration of T_p is applied to the vertex in the direction toward the interface between its two neighboring cells (**Supp. Fig. 5A**). For the analysis of different intercalation types, we simulated the shortening of AP interfaces exclusively and set the filopodial protrusions forming at defined time points (**Fig. 5H**), so that we can distinguish crawling-only intercalation events from concurrent events.

(ii) Contraction at cell cortex.

Contraction at cell cortex is modeled as pieces of Hill's muscle connected in series. The contractile force between two neighboring vertices equals:

$$F_{contract} = \begin{cases} M \cdot f_{stall} \cdot (1 + \dot{\varepsilon}/\dot{\varepsilon_o}), & \dot{\varepsilon} < 0 \\ M \cdot f_{stall} \cdot \left[1 + 0.5 \times \left(1 - e^{-\dot{\varepsilon}/0.5\dot{\varepsilon_o}}\right)\right], & \dot{\varepsilon} \geq 0 \end{cases}$$

, where M is the density of actomyosin, f_{stall} is the stall force, $\dot{\varepsilon}$ is the strain rate in each segment defined by adjacent vertices, and $\dot{\varepsilon_o}$ is the maximum contractile strain rate when force vanishes. To mimic actomyosin pulses long the AP interface (**Fig. 1H**), M is composed of a polarity-dependent baseline of actomyosin M_{base}, plus extra half-sine pulses M_{pulse} in the tricellular regions and/or the middle of the AP interface for a period of T_m (**Supp. Fig. 5A, B**). The extra actomyosin pulses form stochastically in the 4-cell or 27-cell models. However, for the analysis of different intercalation types, we simulated the shortening of AP interfaces exclusively and set the actomyosin pulses at defined time points in tCRs only (**Fig. 5H**), so that we can distinguish contraction-only intercalation events from concurrent events.

(iii) Cell-cell adhesion and force transmission.

Cell-cell adhesion is based on cadherin clustering via its trans- and cis- interaction, and depends on force transmission via cadherin clusters and cadherin-catenin complex binding to the actomyosin network (Lecuit and Yap, 2015) .We simplified cell adhesion as adhesion clusters of the size of $N_{adhesion}$ binding cell edges of adjacent cells, while holding an adhesive force of $F_{adhesion}$ (**Fig. 5C**). The dynamics of adhesion clustering and the adhesion force are interdependent and we used a catch-bond model for the simulation (Buckley et al., 2014; Novikova and Storm, 2013; Rakshit et al., 2012).

Briefly, the force dependent unbinding rate for a single catch-bond can be expressed as $k_u(f) = k_0 \cdot [exp(-f/f^* + \phi_c) + \exp(f/f^* - \phi_s)]$, where k_0 is a reference unbinding rate and set to 1 s^{-1}, f is the force on the bond, f^* is a force scale used to non-dimensionalize all forces, and ϕ_c and ϕ_s represent zero-force unbinding rates associated with the catch and slip portion of the bond dynamics, respectively. Considering an adhesion cluster of the size $N_{adhesion}$ and a tensile load $F_{adhesion}$ uniformly distributed on all bonds, the temporal evolution of the cluster size is expressed as

$$\frac{dN_{adhesion}}{dt} = \gamma \cdot k_0 \cdot \left(N_{adhesion}^{tot} - N_{adhesion}\right) - k_0 \cdot \left[exp\left(-\frac{F_{adhesion}}{N_{adhesion} \cdot f^*} + \phi_c\right) + exp(\frac{F_{adhesion}}{N_{adhesion} \cdot f^*} - \phi_s)\right]$$

, where γ is a dimensionless rebinding rate and $N_{adhesion}^{tot}$ is the polarity-dependent total adhesion units available in the vicinity. Under a quasistatic state, $N_{adhesion}$ and $F_{adhesion}$ can reach their maximum given by $N_{adhesion_max} = \frac{\alpha\gamma}{\alpha\gamma+2} N_{adhesion}^{tot}$ and $F_{adhesion_max} = N_{adhesion_max} \cdot \phi_{max} \cdot f^*$, where $\alpha = exp\ (\phi_s/2 - \phi_c/2)$ and $\phi_{max} = (\phi_s + \phi_{c)}/2$ (see detailed deduction in (Novikova and Storm, 2013).

Clustering is designed to initiate between any vertex-edge pair from two neighboring cells when the distance between them, d is larger than d_r, a repulsion limit defined later to avoid cell collision, but smaller than d_a, the adhesion limit. The two anchoring points of the cluster can move as the cell deforms and can sit anywhere on cell edges.

At the end of each iteration timestep, the adhesive force applied via an adhesion cluster is estimated by $F_{adhesion_e} = k_a \cdot N_{adhesion} \cdot (d - d_r)$, where k_a is the spring constant for a bond unit. k_a is estimated assuming a cluster under a slowly increasing tension reaches its maximum size of $N_{adhesion_max}$ and maximum load of $F_{adhesion_max}$ at d_a, and it equals $k_a = f^* \phi_{max}/d_a$.

(iv) Cytosolic pressure

Cytoplasm is assumed to be linearly elastic, so the difference between the current cell area A and the rest area A_r provides a pressure on cell boundary to maintain the cell size. The cytoplasm potential energy is given by $E_c = \frac{1}{2}\ k_c \left(\frac{A-A_r}{A_r}\right)$, where k_c is the cytoplasm stiffness, and the force on each vertex i can be expressed as

$$F_i = \nabla_i E_c = -k_C \frac{A - A_0}{A_0} \langle y_{i-1} - y_{i+1}, x_{i+1} - x_{i-1} \rangle$$

(v) Contact repulsion

Repulsive forces are applied to any vertex-edge pair from two neighboring cells if the distance between them d if less than d_r or if the vertex is inside the neighboring cell ($d < 0$). The magnitude of this repulsive force is an exponential function of d and is given by

$$F_r = F_{rmax} - (F_{rmax} - F_{r0}) \cdot \exp\left(\frac{d}{d_r} ln \frac{F_{rmax}}{F_{rmax} - F_{r0}}\right)$$

, where F_{r0} is the repulsion at $d = 0$, and F_{rmax} is the maximum repulsion if the vertex is inside a neighboring cell.

References:

Abraham, V.C., V. Krishnamurthi, D.L. Taylor, and F. Lanni. 1999. The actin-based nanomachine at the leading edge of migrating cells. *Biophys J*. 77:1721-1732.

Alt, S., P. Ganguly, and G. Salbreux. 2017. Vertex models: from cell mechanics to tissue morphogenesis. *Philos Trans R Soc Lond B Biol Sci*. 372.

Belmonte, J.M., M.H. Swat, and J.A. Glazier. 2016. Filopodial-Tension Model of Convergent-Extension of Tissues. *PLOS Computational Biology*. 12:e1004952.

Berg, S., D. Kutra, T. Kroeger, C.N. Straehle, B.X. Kausler, C. Haubold, M. Schiegg, J. Ales, T. Beier, M. Rudy, K. Eren, J.I. Cervantes, B. Xu, F. Beuttenmueller, A. Wolny, C. Zhang, U. Koethe, F.A. Hamprecht, and A. Kreshuk. 2019. ilastik: interactive machine learning for (bio)image analysis. *Nat Methods*. 16:1226-1232.

Bertet, C., L. Sulak, and T. Lecuit. 2004. Myosin-dependent junction remodelling controls planar cell intercalation and axis elongation. *Nature*. 429:667-671.

Brieher, W.M., and B.M. Gumbiner. 1994. Regulation of C-cadherin function during activin induced morphogenesis of Xenopus animal caps. *J Cell Biol*. 126:519-527.

Brodland, G.W. 2006. Do lamellipodia have the mechanical capacity to drive convergent extension? *Int J Dev Biol*. 50:151-155.

Buckley, C.D., J. Tan, K.L. Anderson, D. Hanein, N. Volkmann, W.I. Weis, W.J. Nelson, and A.R. Dunn. 2014. The minimal cadherin-catenin complex binds to actin filaments under force. *Science*. 346:1254211.

Butler, M.T., and J.B. Wallingford. 2017. Planar cell polarity in development and disease. *Nat Rev Mol Cell Biol*. 18:375-388.

Chu, C.W., G. Masak, J. Yang, and L.A. Davidson. 2020. From biomechanics to mechanobiology: Xenopus provides direct access to the physical principles that shape the embryo. *Curr Opin Genet Dev*. 63:71-77.

Devitt, C.C., C. Lee, R.M. Cox, O. Papoulas, J. Alvarado, S. Shekhar, E.M. Marcotte, and J.B. Wallingford. 2021. Twinfilin1 controls lamellipodial protrusive activity and actin turnover during vertebrate gastrulation. *Journal of Cell Science*.

Fagotto, F., N. Rohani, A.S. Touret, and R. Li. 2013. A molecular base for cell sorting at embryonic boundaries: contact inhibition of cadherin adhesion by ephrin/ Eph-dependent contractility. *Dev Cell*. 27:72-87.

Fang, X., H. Ji, S.W. Kim, J.I. Park, T.G. Vaught, P.Z. Anastasiadis, M. Ciesiolka, and P.D. McCrea. 2004. Vertebrate development requires ARVCF and p120 catenins and their interplay with RhoA and Rac. *J Cell Biol*. 165:87-98.

Fernandez-Gonzalez, R., M. Simoes Sde, J.C. Roper, S. Eaton, and J.A. Zallen. 2009. Myosin II dynamics are regulated by tension in intercalating cells. *Dev Cell*. 17:736-743.

Finegan, T.M., N. Hervieux, A. Nestor-Bergmann, A.G. Fletcher, G.B. Blanchard, and B. Sanson. 2019. The tricellular vertex-specific adhesion molecule Sidekick facilitates polarised cell intercalation during Drosophila axis extension. *PLOS Biology*. 17:e3000522.

Fletcher, A.G., F. Cooper, and R.E. Baker. 2017. Mechanocellular models of epithelial morphogenesis. *Philos Trans R Soc Lond B Biol Sci*. 372.

Huebner, R.J., A.N. Malmi-Kakkada, S. Sarıkaya, S. Weng, D. Thirumalai, and J.B. Wallingford. 2021a. Mechanical heterogeneity along single cell-cell junctions is driven by lateral clustering of cadherins during vertebrate axis elongation. *eLife*. 10:e65390.

Huebner, R.J., and J.B. Wallingford. 2018. Coming to Consensus: A Unifying Model Emerges for Convergent Extension. *Dev Cell*. 46:389-396.

Huebner, R.J., S. Weng, C. Lee, S. Sarıkaya, O. Papoulas, R.M. Cox, E.M. Marcotte, and J.B. Wallingford. 2021b. Cell adhesions link subcellular actomyosin dynamics to tissue scale force production during vertebrate convergent extension. *bioRxiv*.

Irvine, K.D., and E. Wieschaus. 1994. Cell intercalation during Drosophila germband extension and its regulation by pair-rule segmentation genes. *Development*. 120:827-841.

Keller, R. 2002. Shaping the vertebrate body plan by polarized embryonic cell movements. *Science*. 298:1950-1954.

Keller, R., L.A. Davidson, and D.R. Shook. 2003. How we are shaped: the biomechanics of gastrulation. *Differentiation*. 71:171-205.

Keller, R., and J. Hardin. 1987. Cell behaviour during active cell rearrangement: evidence and speculations. *J Cell Sci Suppl*. 8:369-393.

Keller, R., J. Shih, and A. Sater. 1992. The cellular basis of the convergence and extension of the Xenopus neural plate. *Dev Dyn*. 193:199-217.

Keller, R., and A. Sutherland. 2020. Chapter Ten - Convergent extension in the amphibian, Xenopus laevis. *In* Current Topics in Developmental Biology. Vol. 136. L. Solnica-Krezel, editor. Academic Press. 271-317.

Keller, R., and P. Tibbetts. 1989. Mediolateral cell intercalation in the dorsal, axial mesoderm of Xenopus laevis. *Dev Biol*. 131:539-549.

Kim, H.Y., and L.A. Davidson. 2011. Punctuated actin contractions during convergent extension and their permissive regulation by the non-canonical Wnt-signaling pathway. *J Cell Sci*. 124:635-646.

Lecuit, T., and A.S. Yap. 2015. E-cadherin junctions as active mechanical integrators in tissue dynamics. *Nature Cell Biology*. 17:533-539.

Levayer, R., and T. Lecuit. 2013. Oscillation and polarity of E-cadherin asymmetries control actomyosin flow patterns during morphogenesis. *Dev Cell*. 26:162-175.

Lienkamp, S.S., K. Liu, C.M. Karner, T.J. Carroll, O. Ronneberger, J.B. Wallingford, and G. Walz. 2012. Vertebrate kidney tubules elongate using a planar cell polarity-dependent, rosette-based mechanism of convergent extension. *Nat Genet*. 44:1382-1387.

Martin, A.C., M. Gelbart, R. Fernandez-Gonzalez, M. Kaschube, and E.F. Wieschaus. 2010. Integration of contractile forces during tissue invagination. *J Cell Biol*. 188:735-749.

Merkel, M., and M.L. Manning. 2017. Using cell deformation and motion to predict forces and collective behavior in morphogenesis. *Semin Cell Dev Biol*. 67:161-169.

Miao, H., and J.T. Blankenship. 2020. The pulse of morphogenesis: actomyosin dynamics and regulation in epithelia. *Development*. 147.

Mitrossilis, D., J. Fouchard, A. Guiroy, N. Desprat, N. Rodriguez, B. Fabry, and A. Asnacios. 2009a. Single-cell response to stiffness exhibits muscle-like behavior. *Proceedings of the National Academy of Sciences*. 106:18243-18248.

Mitrossilis, D., J. Fouchard, A. Guiroy, N. Desprat, N. Rodriguez, B. Fabry, and A. Asnacios. 2009b. Single-cell response to stiffness exhibits muscle-like behavior. *Proc Natl Acad Sci U S A*. 106:18243-18248.

Nishimura, T., H. Honda, and M. Takeichi. 2012. Planar cell polarity links axes of spatial dynamics in neural-tube closure. *Cell*. 149:1084-1097.

Novikova, E.A., and C. Storm. 2013. Contractile fibers and catch-bond clusters: a biological force sensor? *Biophys J*. 105:1336-1345.

Petrie, R.J., H. Koo, and K.M. Yamada. 2014. Generation of compartmentalized pressure by a nuclear piston governs cell motility in a 3D matrix. *Science*. 345:1062.

Pfister, K., D.R. Shook, C. Chang, R. Keller, and P. Skoglund. 2016. Molecular model for force production and transmission during vertebrate gastrulation. *Development*. 143:715-727.

Prass, M., K. Jacobson, A. Mogilner, and M. Radmacher. 2006. Direct measurement of the lamellipodial protrusive force in a migrating cell. *J Cell Biol*. 174:767-772.

Rakshit, S., Y. Zhang, K. Manibog, O. Shafraz, and S. Sivasankar. 2012. Ideal, catch, and slip bonds in cadherin adhesion. *Proceedings of the National Academy of Sciences*. 109:18815.

Shih, J., and R. Keller. 1992. Cell motility driving mediolateral intercalation in explants of Xenopus laevis. *Development*. 116:901-914.

Shindo, A. 2018. Models of convergent extension during morphogenesis. *Wiley Interdiscip Rev Dev Biol*. 7.

Shindo, A., Y. Inoue, M. Kinoshita, and J.B. Wallingford. 2019. PCP-dependent transcellular regulation of actomyosin oscillation facilitates convergent extension of vertebrate tissue. *Developmental Biology*. 446:159-167.

Shindo, A., and J.B. Wallingford. 2014. PCP and septins compartmentalize cortical actomyosin to direct collective cell movement. *Science*. 343:649-652.

Sun, Z., C. Amourda, M. Shagirov, Y. Hara, T.E. Saunders, and Y. Toyama. 2017. Basolateral protrusion and apical contraction cooperatively drive Drosophila germ-band extension. *Nat Cell Biol*. 19:375-383.

Tada, M., and C.P. Heisenberg. 2012. Convergent extension: using collective cell migration and cell intercalation to shape embryos. *Development*. 139:3897-3904.

Tamulonis, C., M. Postma, H.Q. Marlow, C.R. Magie, J. de Jong, and J. Kaandorp. 2011. A cell-based model of Nematostella vectensis gastrulation including bottle cell formation, invagination and zippering. *Developmental Biology*. 351:217-228.

Truong Quang, B.A., M. Mani, O. Markova, T. Lecuit, and P.F. Lenne. 2013. Principles of E-cadherin supramolecular organization in vivo. *Curr Biol*. 23:2197-2207.

Uyeda, T.Q.P., Y. Iwadate, N. Umeki, A. Nagasaki, and S. Yumura. 2011. Stretching Actin Filaments within Cells Enhances their Affinity for the Myosin II Motor Domain. *PLOS ONE*. 6:e26200.

Walck-Shannon, E., and J. Hardin. 2014. Cell intercalation from top to bottom. *Nat Rev Mol Cell Biol*. 15:34-48.

Wallingford, J.B., L.A. Niswander, G.M. Shaw, and R.H. Finnell. 2013. The continuing challenge of understanding, preventing, and treating neural tube defects. *Science*. 339:1222002.

Williams, M., W. Yen, X. Lu, and A. Sutherland. 2014. Distinct apical and basolateral mechanisms drive planar cell polarity-dependent convergent extension of the mouse neural plate. *Dev Cell*. 29:34-46.

Zaidel-Bar, R., G. Zhenhuan, and C. Luxenburg. 2015. The contractome – a systems view of actomyosin contractility in non-muscle cells. *Journal of Cell Science*. 128:2209-2217.

Zallen, J.A., and E. Wieschaus. 2004. Patterned gene expression directs bipolar planar polarity in Drosophila. *Dev Cell*. 6:343-355.

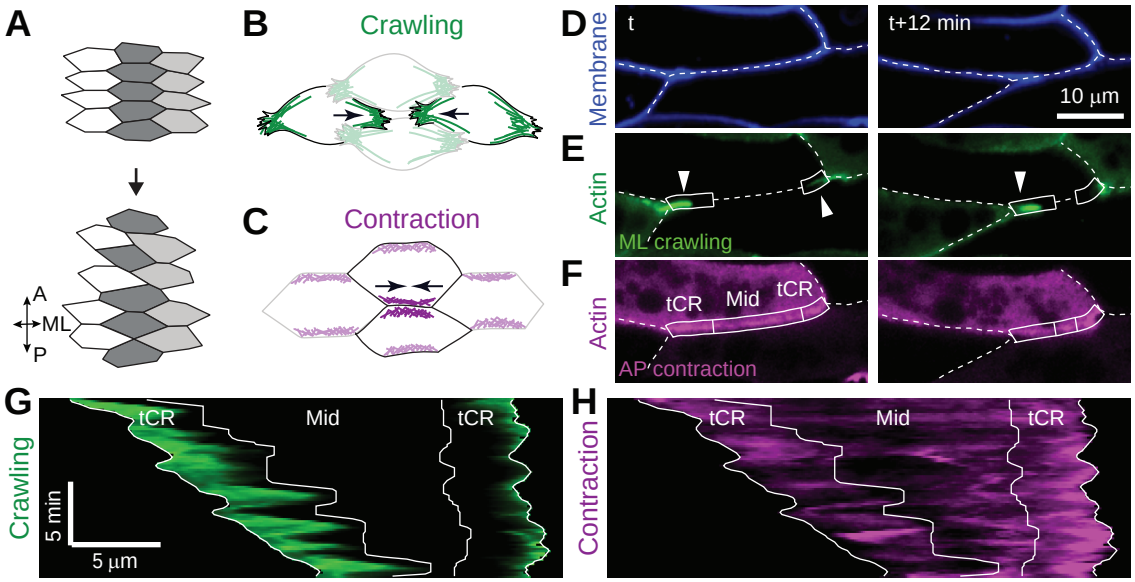

Weng and Wallingford, Figure 1

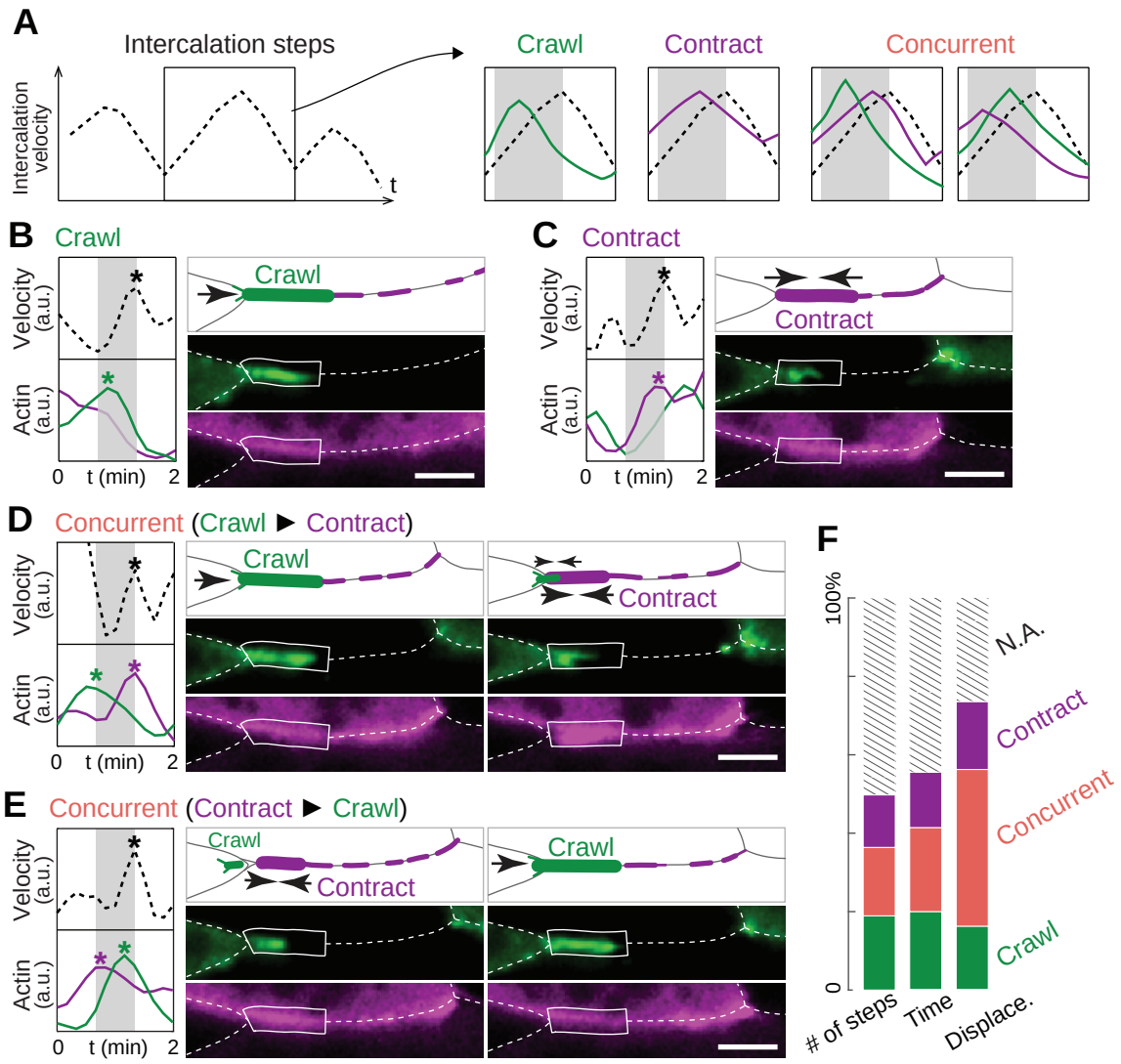

Weng and Wallingford, Figure 2

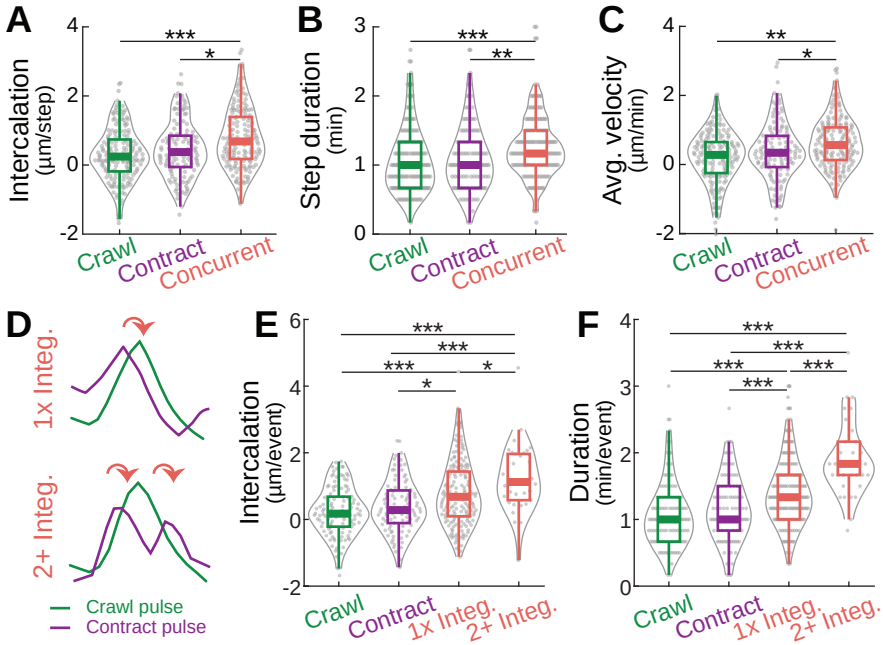

Weng and Wallingford, Figure 3

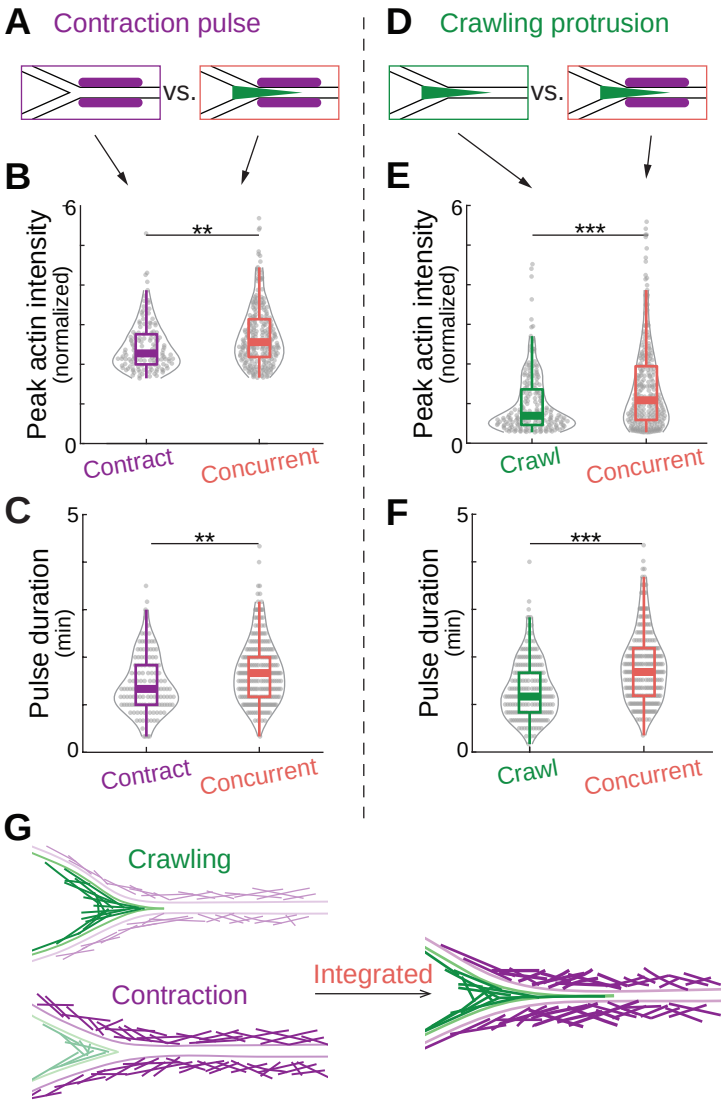

Weng and Wallingford, Figure 4

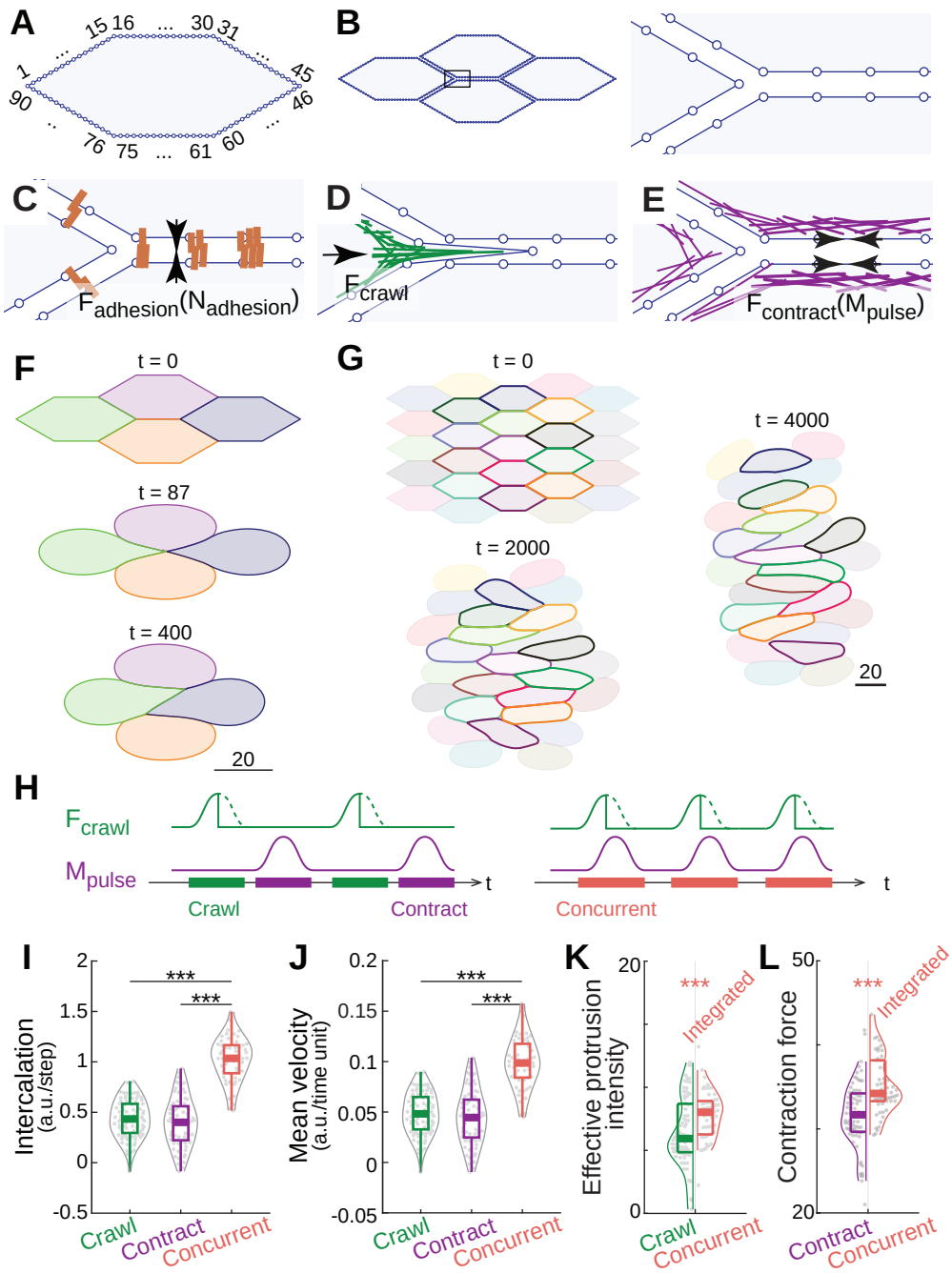

Weng and Wallingford, Figure 5

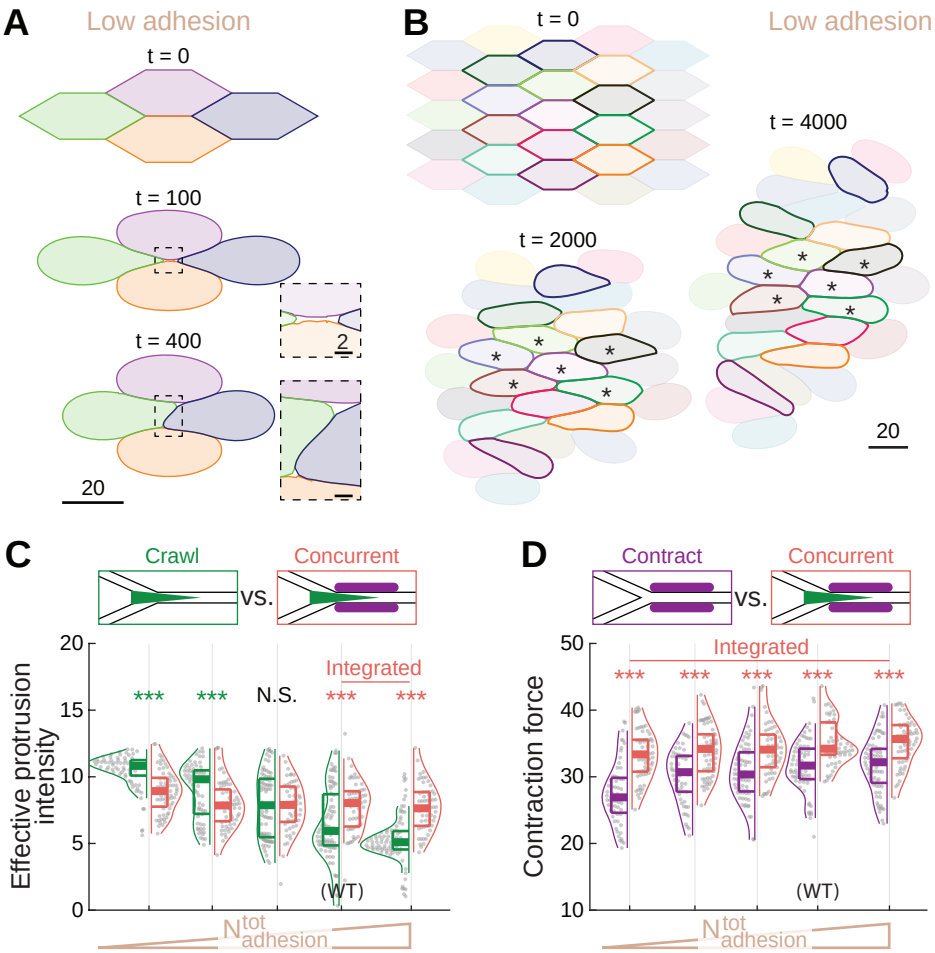

Weng and Wallingford, Figure 6

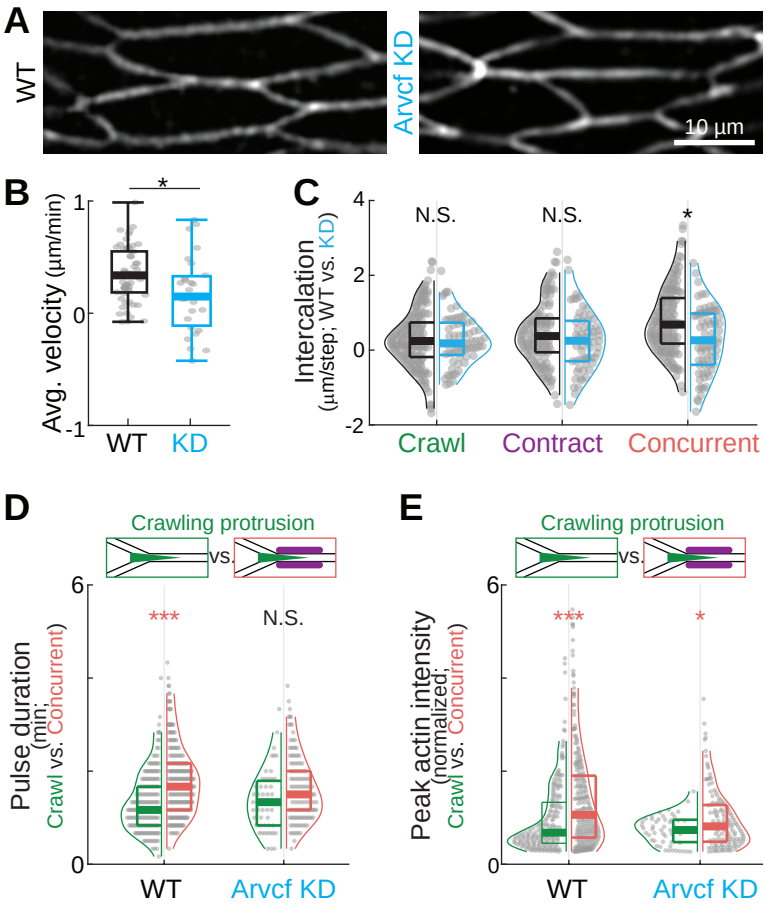

Weng and Wallingford, Figure 7

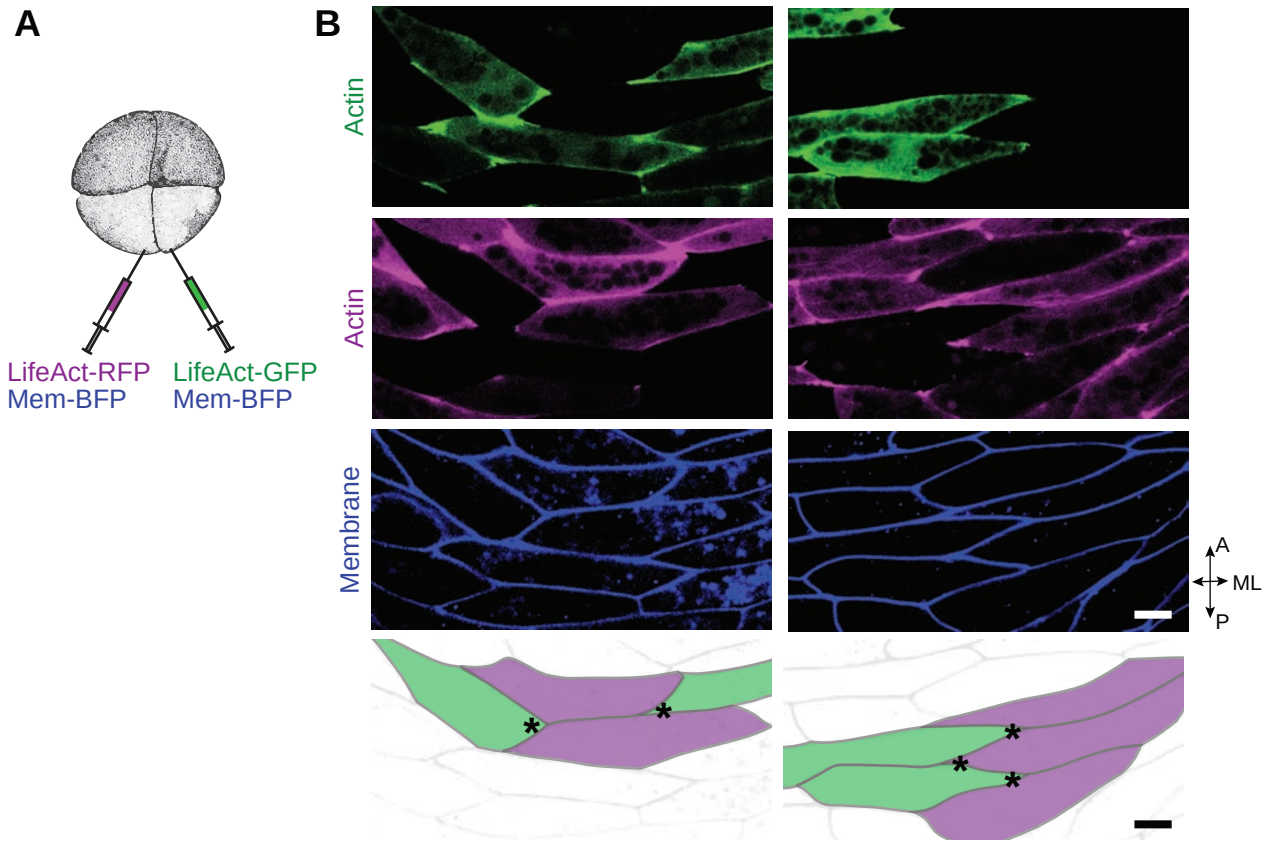

Weng and Wallingford, Supp. Figure 1

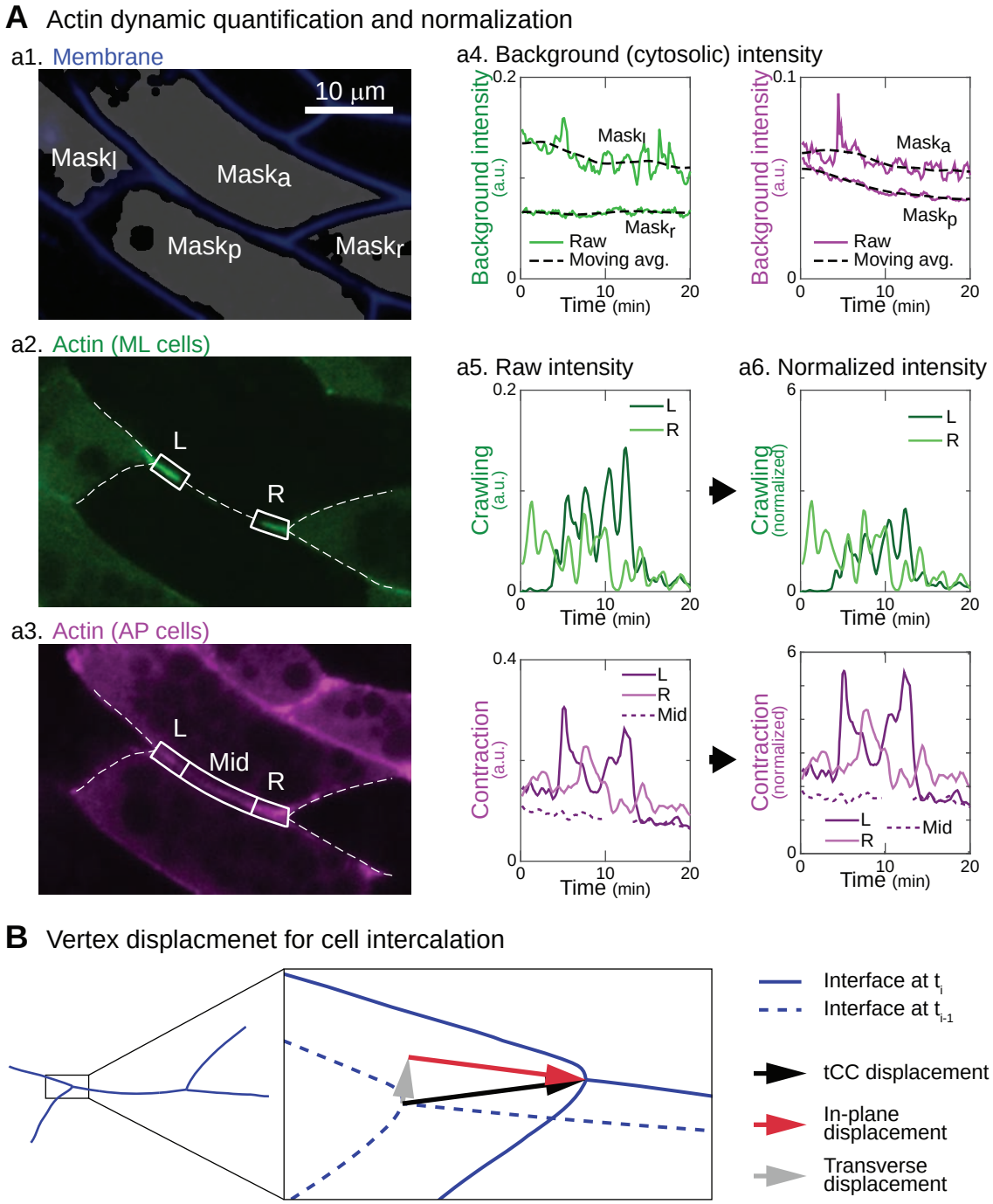

Weng and Wallingford, Supp. Figure 2

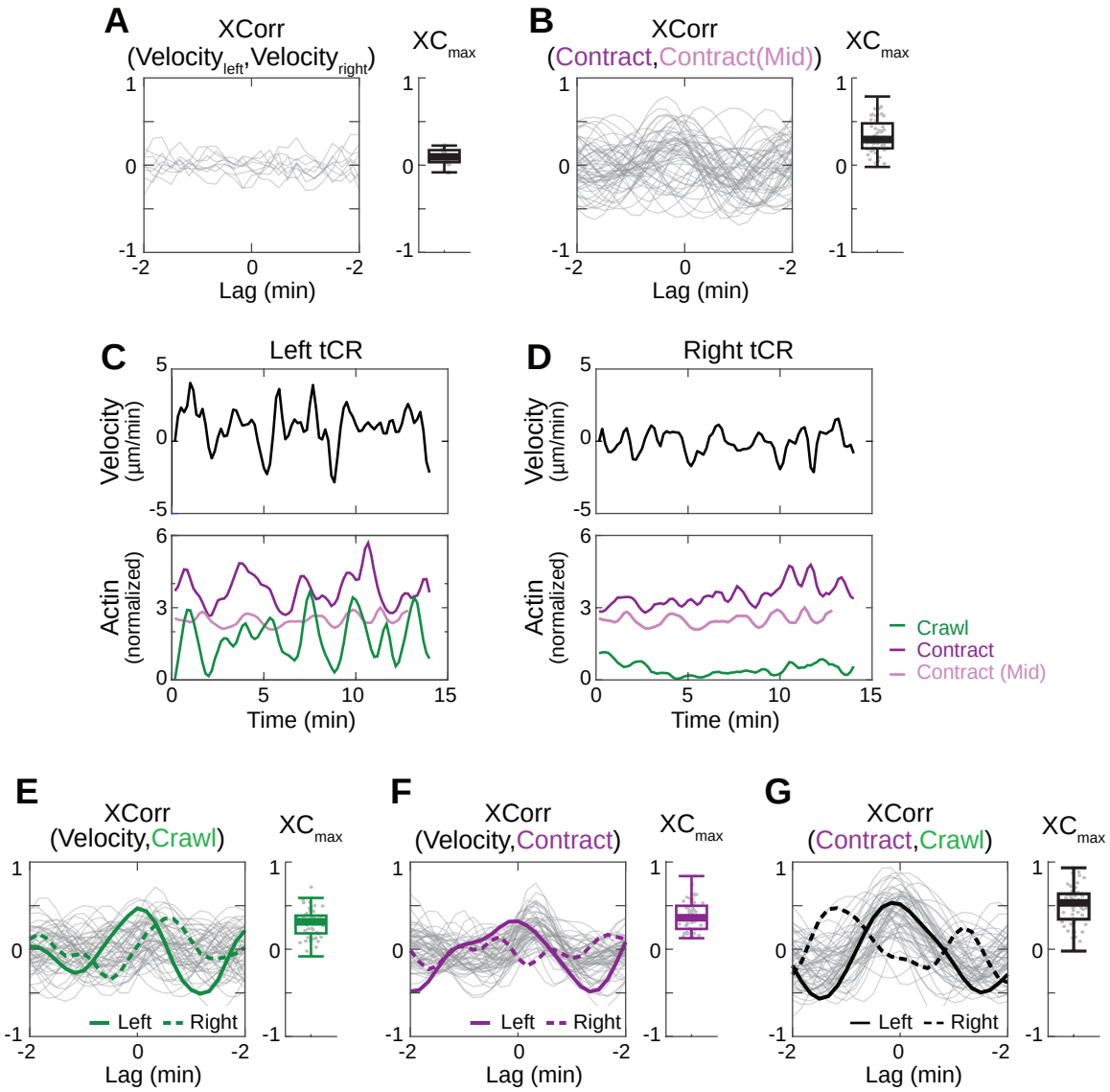

Weng and Wallingford, Supp. Figure 3

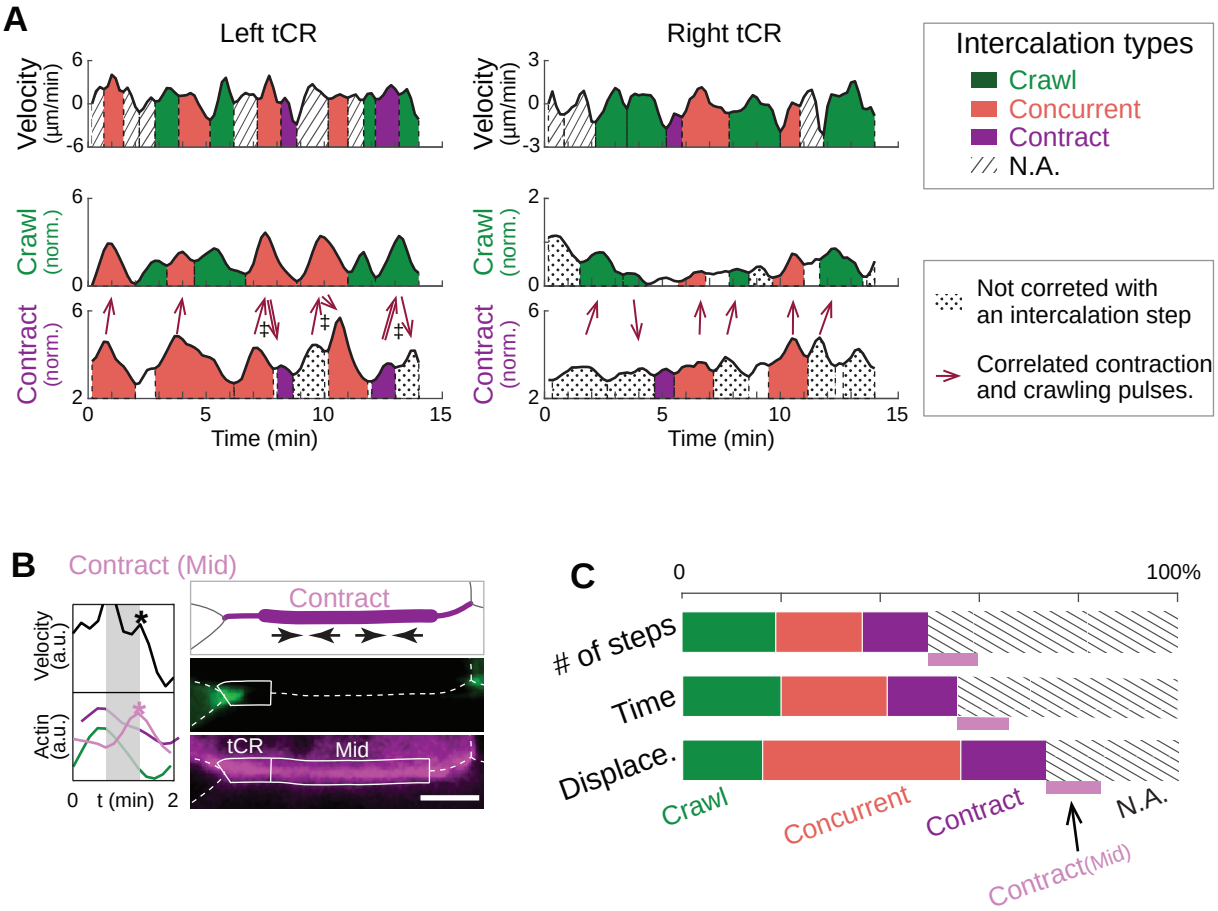

Weng and Wallingford, Supp. Figure 4

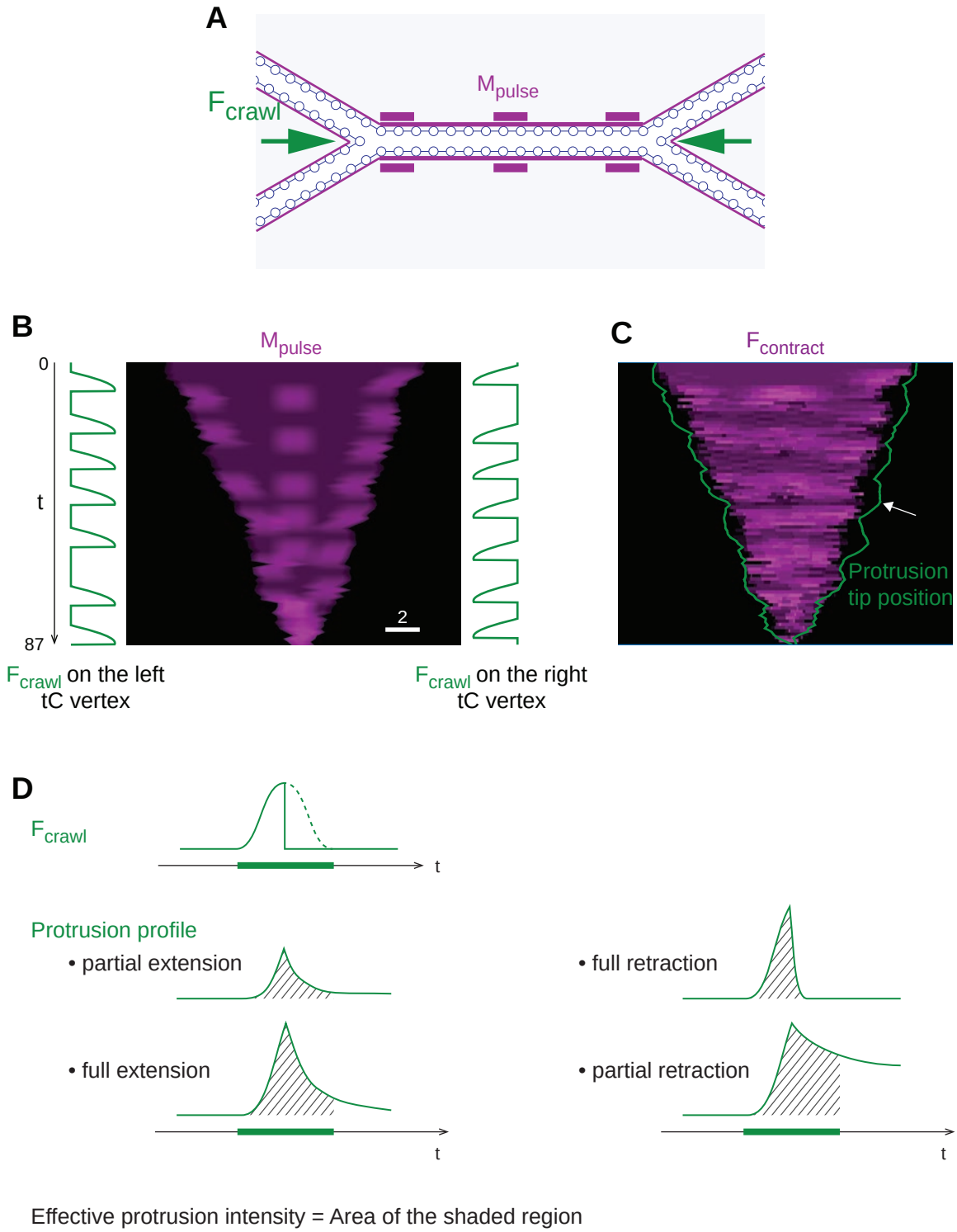

Weng and Wallingford, Supp. Figure 5

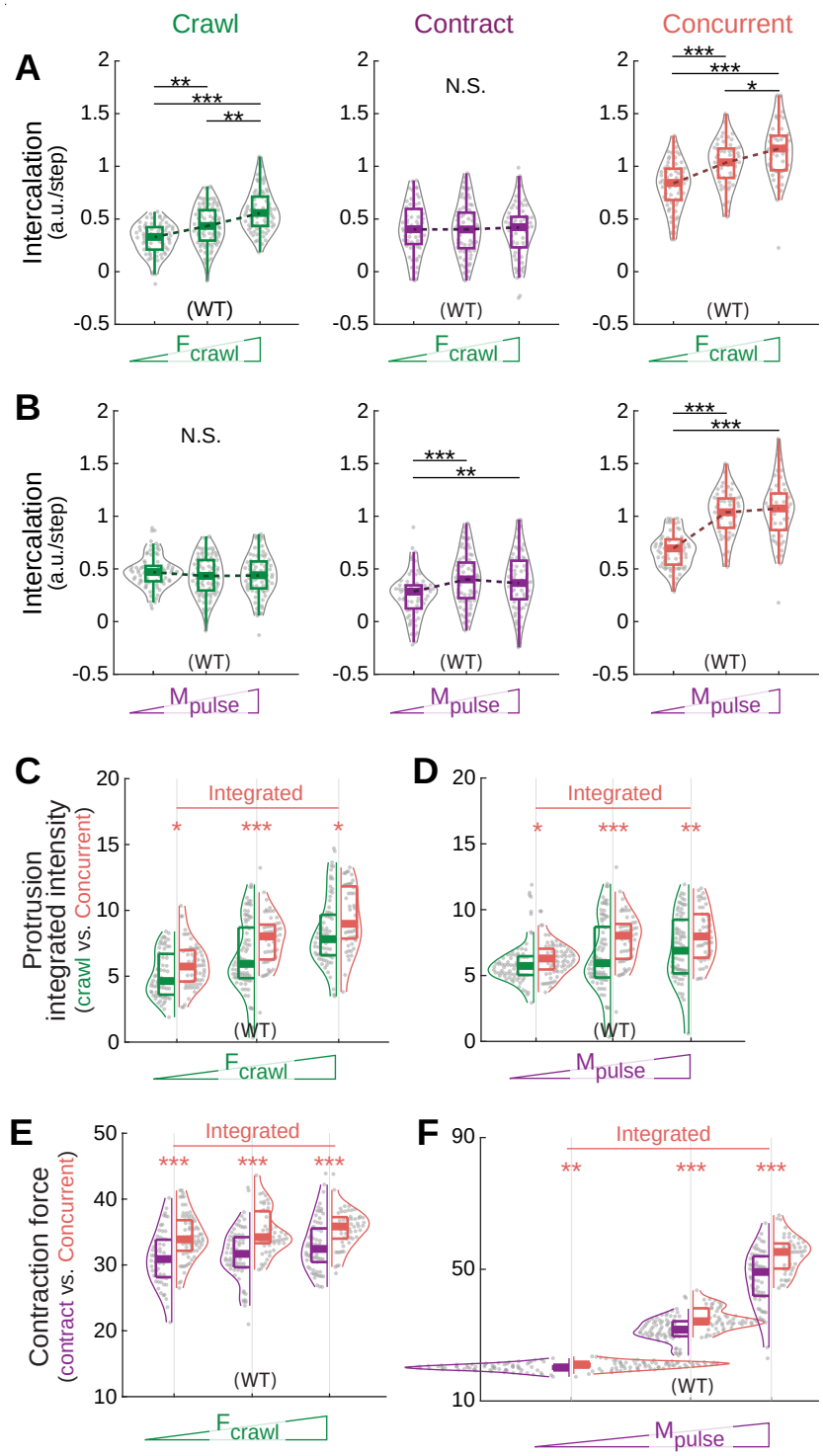

Weng and Wallingford, Supp. Figure 6

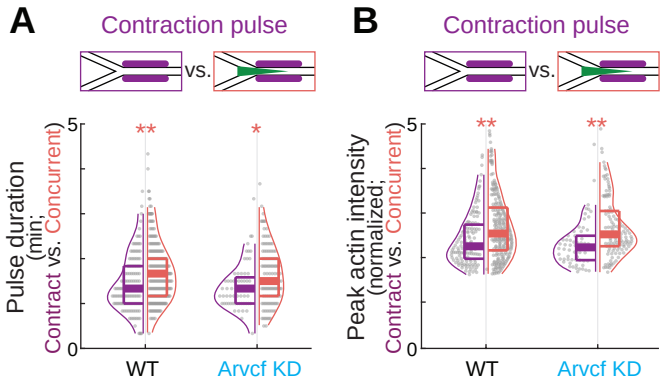

Weng and Wallingford, Supp. Figure 7

Supp. Table 1.

Parameter			Value	Reference
Iteration	Viscosity	η	20	-
	Timestep	Δt	0.05	-
Contraction	Stall force	f_{stall}	4	(Mitrossilis et al., 2009b)
	Actomyosin density	M_{base}	2 (AP) 1 (ML)	(Mitrossilis et al., 2009a)
		M_{pulse}	2, 5*, 8	
	Min. strain rate	$\dot{\varepsilon_o}$	0.8	(Mitrossilis et al., 2009a)
Protrusion	Lamellipodia force	F_l	1	-
	Lamellipodia duration	T_l	100	-
	Protrusion force	F_p	14, 18*, 22	(Abraham et al., 1999; Prass et al., 2006)
	Protrusion duration	T_p	6	-
Adhesion	Force scale	f^*	0.005	(Buckley et al., 2014)
	Catch unbinding rate	ϕ_c	1.0322	(Buckley et al., 2014)
	Slip unbinding rate	ϕ_s	2.9671	(Buckley et al., 2014)
	Rebinding rate	γ	2	-
	Total available adhesion unit	$N_{adhesion}^{tot}$	600†, 800, 1000, 1200*, 1400	(Truong Quang et al., 2013)
		AP/ML	0.6	unpublished data
	Adhesion range	d_a	0.25	-
Cytoplasm	Rest area/Initial area	A_r/A_0	1.002	(Petrie et al., 2014)
	Stiffness	k_C	200	(Petrie et al., 2014)
Repulsion	Maximum force	F_{rmax}	4	-
	Force at zero distance	F_{r0}	1	-
	Repulsion range	d_r	0.025	-

Weng and Wallingford, Supp. Table 1